Tracing Interstellar heating: an ALCHEMI measurement of the HCN Isomers in NGC 253

Behrens, E.; Mangum, J.G.; Holdship, J.R.; Viti, S.; Harada, N.; Martín, S.; ... ; Werf, P.P. van der

Citation

Behrens, E., Mangum, J. G., Holdship, J. R., Viti, S., Harada, N., Martín, S., ... Werf, P. P. van der. (2022). Tracing Interstellar heating: an ALCHEMI measurement of the HCN Isomers in NGC 253. *The Astrophysical Journal*, *939*(2). doi:10.3847/1538-4357/ac91ce

THE ASTROPHYSICAL JOURNAL, 939:119 (26pp), 2022 November 10 https://doi.org/10.3847/1538-4357/ac91ce

Tracing Interstellar Heating: An ALCHEMI Measurement of the HCN Isomers in NGC 253

Erica Behrens[1,19], Jeffrey G. Mangum[2], Jonathan Holdship[3,4], Serena Viti[3,4], Nanase Harada[5,6], Sergio Martín[7,8], Kazushi Sakamoto[9], Sebastien Muller[10], Kunihiko Tanaka[11], Kouichiro Nakanishi[5,6], Rubén Herrero-Illana[7,12], Yuki Yoshimura[13], Rebeca Aladro[14], Laura Colzi[15], Kimberly L. Emig[2,20], Christian Henkel[14,16], Ko-Yun Huang[3], P. K. Humire[14], David S. Meier[17,18], Víctor M. Rivilla[15], and Paul P. van der Werf[3]
(ALMA Comprehensive High-resolution Extragalactic Molecular Inventory (ALCHEMI) Collaboration)
[1] Department of Astronomy, University of Virginia, P.O. Box 400325, 530 McCormick Road, Charlottesville, VA 22904-4325, USA; eb7he@virginia.edu
[2] National Radio Astronomy Observatory, 520 Edgemont Road, Charlottesville, VA 22903-2475, USA
[3] Leiden Observatory, Leiden University, P.O. Box 9513, NL-2300 RA Leiden, The Netherlands
[4] Department of Physics and Astronomy, University College London, Gower Street, London WC1E 6BT, UK
[5] National Astronomical Observatory of Japan, 2-21-1 Osawa, Mitaka, Tokyo 181-8588, Japan
[6] Department of Astronomy, School of Science, The Graduate University for Advanced Studies (SOKENDAI), 2-21-1 Osawa, Mitaka, Tokyo, 181-1855 Japan
[7] European Southern Observatory, Alonso de Córdova, 3107, Vitacura, Santiago 763-0355, Chile
[8] Joint ALMA Observatory, Alonso de Córdova, 3107, Vitacura, Santiago 763-0355, Chile
[9] Institute of Astronomy and Astrophysics, Academia Sinica, 11F of AS/NTU Astronomy-Mathematics Building, No.1, Sec. 4, Roosevelt Road, Taipei 10617, Taiwan
[10] Department of Space, Earth and Environment, Chalmers University of Technology, Onsala Space Observatory, SE-43992 Onsala, Sweden
[11] Department of Physics, Faculty of Science and Technology, Keio University, 3-14-1 Hiyoshi, Yokohama, Kanagawa 223–8522 Japan
[12] Institute of Space Sciences (ICE, CSIC), Campus UAB, Carrer de Magrans, E-08193 Barcelona, Spain
[13] Institute of Astronomy, Graduate School of Science, The University of Tokyo, 2-21-1 Osawa, Mitaka, Tokyo 181-0015, Japan
[14] Max-Planck-Institut für Radioastronomie, Auf dem Hügel 69, D-53121 Bonn, Germany
[15] Centro de Astrobiología (CSIC-INTA), Ctra. de Ajalvir Km. 4, SE-28850, Torrejón de Ardoz, Madrid, Spain
[16] Astronomy Department, Faculty of Science, King Abdulaziz University, P.O. Box 80203, Jeddah 21589, Saudi Arabia
[17] New Mexico Institute of Mining and Technology, 801 Leroy Place, Socorro, NM 87801, USA
[18] National Radio Astronomy Observatory, PO Box O, 1003 Lopezville Road, Socorro, NM 87801, USA

Received 2022 May 6; revised 2022 August 30; accepted 2022 September 12; published 2022 November 14

Abstract

We analyze HCN and HNC emission in the nearby starburst galaxy NGC 253 to investigate its effectiveness in tracing heating processes associated with star formation. This study uses multiple HCN and HNC rotational transitions observed using the Atacama Large Millimeter/submillimeter Array via the ALCHEMI Large Program. To understand the conditions and associated heating mechanisms within NGC 253's dense gas, we employ Bayesian nested sampling techniques applied to chemical and radiative transfer models, which are constrained using our HCN and HNC measurements. We find that the volume density n_{H_2} and cosmic-ray ionization rate (CRIR) ζ are enhanced by about an order of magnitude in the galaxy's central regions as compared to those further from the nucleus. In NGC 253's central giant molecular clouds (GMCs), where observed HCN/HNC abundance ratios are the lowest, $n \sim 10^{5.5}$ cm^{-3} and $\zeta \sim 10^{-12}$ s^{-1} (greater than 10^4 times the average Galactic rate). We find a positive correlation in the association of both density and CRIR with the number of star formation-related heating sources (supernova remnants, H II regions, and super hot cores) located in each GMC, as well as a correlation between CRIRs and supernova rates. Additionally, we see an anticorrelation between the HCN/HNC ratio and CRIR, indicating that this ratio will be lower in regions where ζ is higher. Though previous studies suggested HCN and HNC may reveal strong mechanical heating processes in NGC 253's CMZ, we find cosmic-ray heating dominates the heating budget, and mechanical heating does not play a significant role in the HCN and HNC chemistry.

Unified Astronomy Thesaurus concepts: Starburst galaxies (1570); Cosmic rays (329); Star formation (1569); Star forming regions (1565); Active galaxies (17); Astrochemistry (75); Galaxy nuclei (609); Spiral galaxies (1560); Interstellar molecules (849)

Supporting material: machine-readable table

1. Introduction

Starburst galaxies have long been subjects of interest in astrophysical research due to their extreme star-forming environments as compared to the Milky Way. Observing starburst galaxies allows us to study how stars form in regions with higher densities, temperatures, and velocity dispersion. However, the physical conditions in extragalactic star-forming regions are not well understood due to limitations in resolving substructure and thus examining conditions on giant molecular cloud (GMC) scales at millimeter and submillimeter wavelengths (Leroy et al. 2018). Many processes associated with star formation (mechanical heating in the form of shocks and turbulence from supernova explosions, radiative heating from massive stars, ionization by cosmic rays from supernova remnants, etc.) have competing effects on the interstellar medium (ISM). Determining the influence of each of these physical

---

[19] Student at the National Radio Astronomy Observatory.
[20] Jansky Fellow of the National Radio Astronomy Observatory.

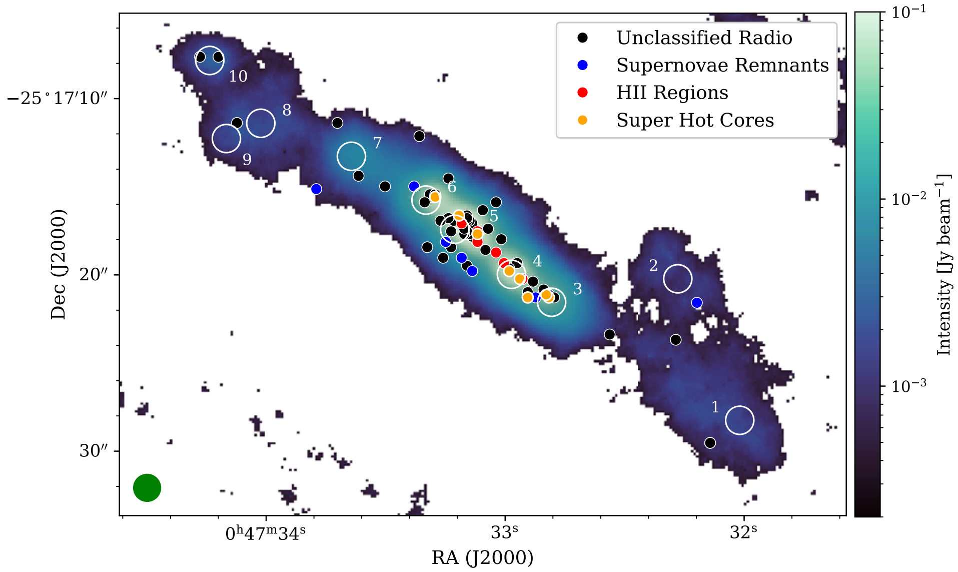

Figure 1. Location of radio continuum sources (Ulvestad & Antonucci 1997) and super hot cores (Rico-Villas et al. 2020) within the NGC 253 CMZ plotted over the 212 GHz ALCHEMI dust continuum emission. Numbered white circles indicate GMCs identified in Leroy et al. (2015). The beam size of 1.″6 is shown by the green circle in the bottom left corner.

processes on extragalactic star-forming regions is crucial to our understanding of the chemical and physical processes that guide star formation in starburst environments.

We study the nearby galaxy NGC 253 as a laboratory for exploring how the current generation of stars affects future star formation in a starburst galaxy. It has an inclination of 76° (McCormick et al. 2013), and at a distance of 3.5 ± 0.2 Mpc (Rekola et al. 2005), NGC 253 is an ideal target for studying extragalactic star formation. NGC 253 features a central molecular zone (CMZ) spanning ∼800 pc across which hosts at least 10 GMCs identified via the dense gas tracers HCN, HCO^+, and CS (Leroy et al. 2015, Appendix A and Figure 1). Despite hosting a star formation rate of 5 $M_\odot$ yr^{-1} across the entire galaxy, the central kiloparsec accounts for 40% of that rate, forming stars at a rate of 2 $M_\odot$ yr^{-1}. This centrally concentrated star formation results in NGC 253's classification as a nuclear starburst (Leroy et al. 2015).

To capitalize on NGC 253's ideal positioning and chemical complexity (Aladro et al. 2015; Martín et al. 2019), the ALMA Comprehensive High Resolution Molecular Inventory (ALCHEMI) observing program was conducted. ALCHEMI is an Atacama Large Millimeter/submillimeter Array (ALMA) large program that imaged the NGC 253 CMZ over a frequency range of 84.2–373.2 GHz (Martín et al. 2021). ALCHEMI has cultivated the investigation of the rich chemical environment within the NGC 253 CMZ using a comprehensive molecular inventory to trace chemical and physical processes associated with starburst environments. ALCHEMI allows for the study of GMC-scale structures (∼50 pc) located in NGC 253's CMZ due to its sensitivity to physical size scales from 255 pc (15″) to 28 pc (1.″6).

This paper is one in a series of ALCHEMI projects that analyzes the conditions in the NGC 253 CMZ using molecular signatures (Martín et al. 2021; Harada et al. 2021; Holdship et al. 2021; Haasler et al. 2022; Holdship et al. 2022; Humire et al. 2022). Additionally, in this paper we explore how molecular emission can trace heating processes associated with star formation in this active environment.

The strong star formation activity in NGC 253 is evidenced by at least 64 individual compact radio continuum sources within the CMZ (Ulvestad & Antonucci 1997), particularly concentrated in GMCs 3–6 (Figure 1). Ulvestad & Antonucci (1997) measure spectral indices α ($S_\nu \propto \nu^\alpha$) for 23 of these sources using wavelengths ranging from 1.3–20 cm with resolutions between 1 and 15 pc. Of these 23 spectral index measurements, 17 have spectral index uncertainties σ_α of less than 0.4. About half of the sources in this subset are believed to be supernova remnants due to a measured spectral index below −0.4, which is indicative of synchrotron radiation. The remaining usable sources with $\sigma_\alpha < 0.4$ have spectral indices α ranging from 0.0–0.2, which is consistent with free–free emission from H II regions. Ulvestad & Antonucci (1997) note that the majority of sources emitting free–free radiation lie along the galaxy disk's major axis, whereas the synchrotron sources lie farther away from the midline. The brightest of these radio sources (TH2, Turner & Ho 1985) is located in GMC 5 and associated with the nucleus of the galaxy, within 1″ of the galaxy's kinematic center (Müller-Sánchez et al. 2010). Other sources associated with star formation in the CMZ are proto-super star clusters (Leroy et al. 2018) containing super hot cores identified by Rico-Villas et al. (2020)[21] using vibrationally excited HC_3N emission. These measurements suggest that the NGC 253 CMZ GMCs are currently at different stages of evolution.

2. HCN and HNC in Galaxies

To investigate the physical conditions in the NGC 253 CMZ, we can use combinations of chemical tracers from ALCHEMI's robust data set that highlight the mechanisms involved in star formation and its effects on the environment. The combination that we will explore in this article is HCN and its isomer HNC. HCN and HNC have similar energy level structures and dipole moments (differ by 2.2%); hence, their

---

[21] Note that the measurements identifying super hot cores sample only the part of the NGC 253 CMZ encompassing GMCs 3–6.

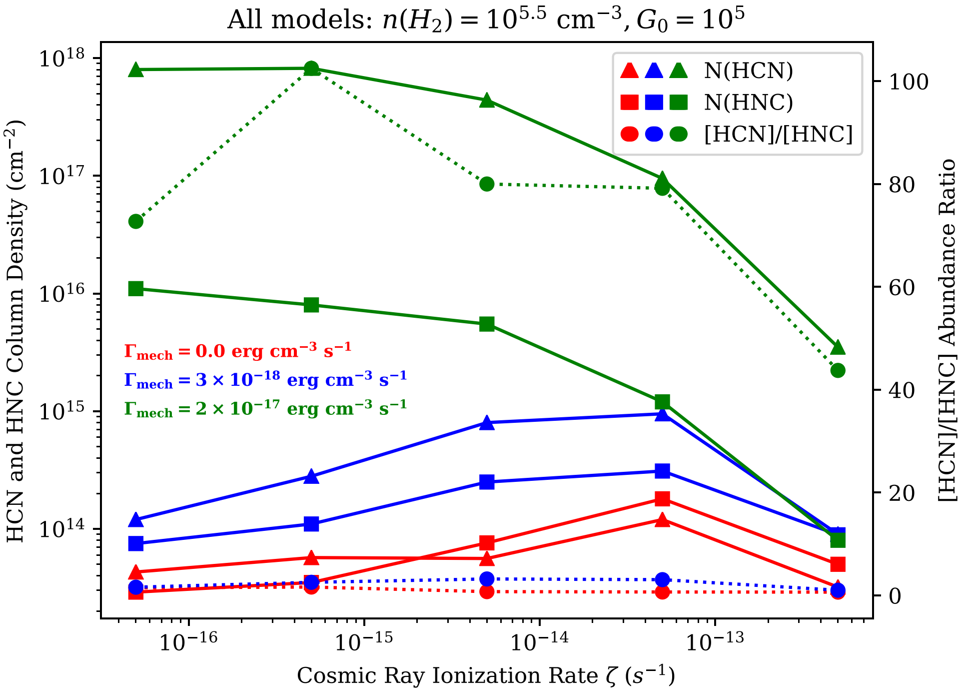

Figure 2. HCN and HNC column density (left axis) and column density ratio (right axis) as a function of CRIR ζ and mechanical heating rate $\Gamma_{\rm mech}$ from the PDR models presented by Meijerink et al. (2011). Volume density $n_{\rm H_2}$ and far-UV radiation field intensity G$_0$ are fixed at $10^{5.5}$ cm^{-3} and 10^5 Habing, respectively, in these models.

abundance ratio is often used as a probe of gas chemical conditions (e.g., Goldsmith et al. 1986; Schilke et al. 1992; Herbst et al. 2000).

Additionally, HCN and HNC transitions are relatively bright in an extragalactic context and thus easy to detect. Studies of the HCN and HNC emission have been reported on a wide range of galaxy types, including normal, luminous infrared, and active galactic nucleus-dominated galaxies (Aalto et al. 2002, 2007a, 2007b; Pérez-Beaupuits et al. 2007; Greve et al. 2009; Costagliola et al. 2011; Kamenetzky et al. 2011; Aalto et al. 2012; Imanishi & Nakanishi 2013; Costagliola et al. 2015; Green et al. 2016; Li et al. 2021), as well as high-redshift galaxies (Spilker et al. 2014). Using HCN and HNC transitions ranging from $J = 1$–0 to 4–3 the HCN/HNC spectral line integrated intensity ratio ranges from ∼1–5. In a few luminous infrared galaxies, the HCN/HNC spectral line intensity ratio is measured to be less than 1 (Aalto et al. 2007b). In these galaxies, a model that includes infrared excitation of the lowest-energy vibrational bending mode is used to explain this unusual HCN/HNC ratio.

In our own Galaxy, the HCN/HNC ratio is very close to unity across different environments, from dense quiescent molecular clouds to star-forming regions (e.g., Irvine & Schloerb 1984; Hirota et al. 1998). Within the low-A_v and high-UV flux environments found in planetary nebulae, HNC is more readily destroyed due to the warming of the environment from UV radiation (Bublitz et al. 2022). However, in high-A_v regions where high-mass star formation dominates, the HCN/HNC abundance ratio has been found to be much higher (Schilke et al. 1992). This is believed to be due to the destruction of HNC (rather than an enhancement of HCN) via an isomerization reaction that occurs at relatively high temperatures. However, the temperature barrier for this reaction is uncertain. Theoretical studies suggest a barrier of 1200 K, while observational results are better explained by a 200 K barrier (Graninger et al. 2014; Hacar et al. 2020). Despite these conflicting results, it would be expected that at high temperatures, the abundance of HCN would increase with respect to HNC.

Previous studies have used ratios of formaldehyde transitions to derive kinetic temperatures $T_{\rm K}$ in NGC 253's central GMCs (3–7), finding that $T_K \gtrsim 50$ K on 5″ (∼80 pc) scales and $T_K \gtrsim 300$ K on $\lesssim 1''$ ($\lesssim$16 pc) scales (e.g., Mangum et al. 2019). It is unclear exactly which mechanisms are raising the kinetic temperatures to this level, but one possible explanation is mechanical heating as a result of shocks generated by supernova explosions and cloud-cloud collisions, as well as outflows from young stars (Mauersberger et al. 2003). Meijerink et al. (2011) suggest that mechanical heating consistent with the star formation activity in starburst galaxies could raise temperatures to over 100 K and up to 1000 K in regions of lower column density ($\lesssim 5 \times 10^{21}$ cm^{-2}) for volume densities of $10^{5.5}$ cm^{-3}. Meijerink et al. (2011) also find that mechanical heating that would raise the kinetic temperature to such values could increase the HCN/HNC abundance ratio by up to two orders of magnitude compared to its Milky Way value in quiescent clouds, suggesting that this ratio could be a good mechanical heating indicator (Figure 2). Kazandjian et al. (2012) echo these results. Hacar et al. (2020) propose using the HCN/HNC abundance ratio as a kinetic temperature probe.

Alternatively, cosmic rays, without the addition of mechanical heating, could be responsible for the kinetic temperatures measured in NGC 253's CMZ (Papadopoulos 2010; Bayet et al. 2011). However, high rates of cosmic-ray ionization may depress the HCN/HNC abundance ratio, as suggested by the analyses presented in Bayet et al. (2011) and Meijerink et al. (2011, Figure 2), which predict HCN and HNC abundances as a function of cosmic-ray ionization rate (CRIR).

Table 1
HCN Isomer Measurements

Transition	HCN, HNC	
$J-(J-1)$	Frequency (GHz)	$\sigma_{\rm chan}$ (mJy beam^{-1})
1–0	88.632, 90.664	0.27, 0.26
2–1	177.261, 181.325	6.41, 12.52
3–2	265.886, 271.981	1.46, 1.98
4–3	354.505, 362.630	2.70, 3.47

It is important to note, however, that these studies used models that couple temperature and chemical abundance calculations, where CRIR affects the temperature. Thus, the effect of cosmic-ray ionization and cosmic-ray heating of the gas are difficult to separate. In order to fully differentiate between the contributions of cosmic-ray chemistry and cosmic-ray heating on the molecular ISM, we treat cosmic rays and heating separately in our models.

Our work combines ALCHEMI observations with chemical and physical modeling in order to ascertain the mechanisms driving the high kinetic temperatures in the nucleus of NGC 253. In Section 3, we describe our ALCHEMI HCN and HNC isomer observations. We present the methods and results of our chemical modeling analysis in Section 4. Section 5 discusses the implications of our combined observational and modeling results, and we summarize our findings in Section 6.

3. Observational Data

3.1. ALCHEMI Data

In the following we provide a summary of the observation setup used to acquire the ALCHEMI survey data. Full details regarding the data acquisition, calibration, and imaging are provided in Martín et al. (2021). The ALMA Cycle 5 Large Program ALCHEMI (project code 2017.1.00161.L) imaged the CMZ within NGC 253 in the ALMA frequency Bands 3, 4, 6, and 7. This survey was subsequently extended to Band 5 during ALMA Cycle 6 (project code 2018.1.00162.S). The nominal phase center of the observations is α(ICRS) = $00^{\rm h}47^{\rm m}33^{\rm s}.26$, δ(ICRS) = $-25°17'17''.7$. A common rectangular area that was $50'' \times 20''$ (850×340 pc) at a position angle of 65° (east of north) represented the nuclear region (CMZ) imaged in NGC 253. The final angular and spectral resolution of the image cubes generated from these measurements were $1''.6$ (∼27 pc) and 8–9 km s^{-1}, respectively (Martín et al. 2019). The combination of the 12 m Array and Atacama Compact Array measurements used in this analysis resulted in a common maximum recoverable angular scale of $15''$ at all frequencies. The rest-frequency coverage of ALCHEMI ranged from 84.2–373.2 GHz.

From the ALCHEMI archive, we extract the $\sim 1''.6$ resolution mosaics of the CMZ of NGC 253 in the HCN and HNC 1–0, 2–1, 3–2, and 4–3 rotational transitions. Table 1 lists the transitions, frequencies, and spectral channel rms values for all measurements studied. We also extract the continuum emission associated with the measurements listed in Table 1. The continuum subtraction and imaging processes used in this analysis are described in Martín et al. (2021).

3.2. Spectral Line Signal Extraction

In order to extract integrated spectral line intensities from our measurements, we use the `CubeLineMoment`[22] script introduced for this same purpose by Mangum et al. (2019). `CubeLineMoment` uses a series of spectral and spatial masks to extract integrated intensities for a defined list of target spectral frequencies. As noted by Mangum et al. (2019), the `CubeLineMoment` masking process uses a bright spectral line whose velocity structure is representative of the emission over the galaxy as a *tracer* of the gas under study. As the HCN and HNC emission measured toward NGC 253 is quite intense in all transitions we were able to use each as its own tracer. Final moment 0 (integrated intensity; jansky per kilometer per second), 1 (average velocity; kilometer per second), and 2 (velocity dispersion; kilometer per second) images are generated using a signal limit of three times the spectral channel baseline rms for the respective transition under study.

The moment-0 images for all HCN and HNC transitions are shown in Figures 3 and 4. Ratios of each moment-0 HCN isomer for each transition have also been calculated (Figure 5).

To obtain integrated intensity values from across the CMZ while taking into account the limits of our resolution, we average the integrated intensity emission inside each of the 10 GMC-like structures identified by Leroy et al. (2015). Leroy et al. (2015) define a GMC as an overdensity in molecular line emission on scales of ∼50 pc. Using this definition, Leroy et al. (2015) identify 10 GMCs in the NGC 253 CMZ (Table A1), though these clouds are noted to have higher densities ($n_{\rm H_2} \sim 2000$ cm^{-3} over a three-dimensional GMC-sized FWHM) and line widths ($\sigma \sim 20$–40 km s^{-1}) than GMCs found in our own Galaxy.

We extract HCN and HNC integrated intensities for each of the four transitions and average each of them over these GMCs, adopting diameters equal to our beam size ($1''.6$, which is much smaller than the maximum recoverable angular scale of $15''$ for the ALCHEMI image cubes). Though we do not center these GMCs on peaks in the HCN and HNC emission, we find that the emission is smooth enough that any potential offset between the centers of the two species' emissions would not substantially affect our calculated integrated intensities. Any remaining dilution of the HCN and HNC emission when averaging over the chosen GMC positions will underestimate the intensity of that emission. Uncertainties are calculated taking into account spectral channel rms values, line widths, and absolute flux calibration uncertainties (Martín et al. 2021) for each integrated intensity measurement. A list of the GMC-averaged integrated intensities is shown in Table 2.

These measurements suggest that the HCN/HNC integrated intensity ratio for all four transitions ranges from 1–5 (Figure 5), which is similar to that measured toward a wide range of galaxy types (Section 2). These ratios are at their lowest (∼1–2) in the central region of the CMZ, which encompasses GMCs 3–6.

3.3. Interloper Analysis

Our `CubeLineMoment` analysis includes a sample spectrum check to reveal potential spectral line blending. Only the HNC 4–3 transition is found to have spectral neighbors, which required assessment of the amount of emission contributed by

---

[22] https://github.com/keflavich/cube-line-extractor

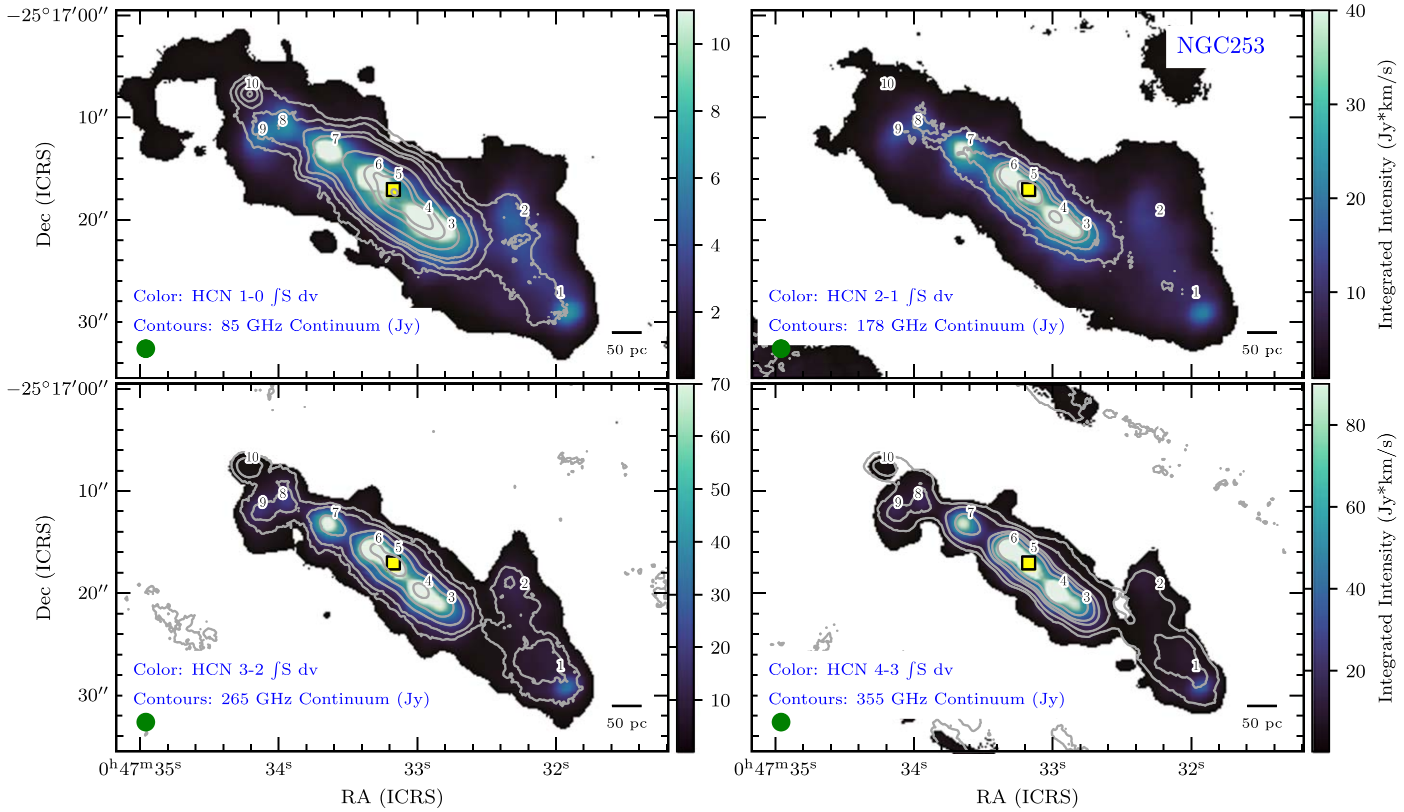

Figure 3. HCN integrated intensity (moment-0) images toward NGC 253. For each image, the green circle in the lower-left corner shows the final imaged beam size (1.″6). White-bordered numbers indicate the locations of the dense molecular emission regions identified by Leroy et al. (2015, Table 4). The yellow black-bordered square locates the position of the strongest radio continuum emission peak identified by Turner & Ho (1985b, TH2: R.A.(J2000) = $00^h47^m33^s.18$, Decl. (J2000) = −25°17′16.″93). A scale bar in the lower right of each panel provides the physical scale in parsecs for each image. The lower integrated intensity limit for each transition is set to 3σ (see Table 1). Overlaid in contours is the associated continuum emission distribution for each transition. Continuum contours are in steps of 3, 6, 9, 12, 30, 120, 240, and 900 times the respective continuum rms, where the peak continuum intensity dictates the number of these levels actually used for a given panel. The respective continuum rms values for the transitions shown are 0.07, 1.5, 0.3, and 1.0 mJy beam^{-1}.

H_2CO 5_{05}–4_{04} (362.736048 GHz) and HNC 4–3 $v_2 = 1$ (362.554351 GHz). Using the procedure described in Holdship et al. (2022) we determine that these two interlopers contribute, respectively, at most 4% and 1% to the HNC 4–3 integrated emission. This contamination estimate is consistent with the multispecies LTE analysis of molecular column densities described in Martín et al. (2021). Figure 6 shows a sample spectrum toward a central region in the NGC 253 CMZ (Region 6), which indicates the spectral line blending of the HNC 4–3 transition. Since the estimated correction required for this single transition is small, we do not apply these corrections to our presented integrated intensities.

4. Coupled Radiative Transfer—Chemical Modeling

4.1. Model Description

We model the chemical and physical conditions within each of the 10 GMCs using the chemical modeling code `UCLCHEM`[23] (Holdship et al. 2017) and the radiative transfer code `SpectralRadex`.[24]

`UCLCHEM` is a gas-grain chemical modeling code that incorporates user-defined chemical networks to produce chemical abundances given the input physical conditions of the gas (e.g., gas temperature, volume density). We take our gas phase network from UMIST12 (McElroy et al. 2013), which includes two-body reactions between species as well as reactions with UV photons and cosmic rays, and use depleted abundances from Table 4 of Jenkins (2009) for our initial conditions. The cosmic-ray reaction rates use a CRIR of $\zeta_0 = 1.36 \times 10^{-17}$ s^{-1} from which the CRIRs are scaled. We augment this database by including the reaction,

$$\mathrm{HNC} + \mathrm{O} \longrightarrow \mathrm{CO} + \mathrm{NH}, \tag{1}$$

which has been shown to be important in the chemistry of HCN and HNC (Hacar et al. 2020). The isomerization reaction that converts HNC into HCN is already included in the database:

$$\mathrm{HNC} + \mathrm{H} \longrightarrow \mathrm{HCN} + \mathrm{H}. \tag{2}$$

We test both the high (2000, 1200 K) and low (20, 200 K) barrier values (Hacar et al. 2020) for the HNC + O and HNC + H reactions in order to understand the effects of temperature barriers on our modeling results. We further include `UCLCHEM`'s default grain surface reactions including freeze-out, nonthermal desorption, and diffusive reactions between species adsorbed to the grain. We use a single-point model to replicate the environment in the GMCs by assuming these gas clouds are homogeneous because they have high enough visual extinctions such that they are shielded from UV radiation (Harada et al. 2021). We calculate the species column density using the on-the-spot approximation, where we multiply the fractional

---

[23] https://uclchem.github.io/

[24] https://spectralradex.readthedocs.io

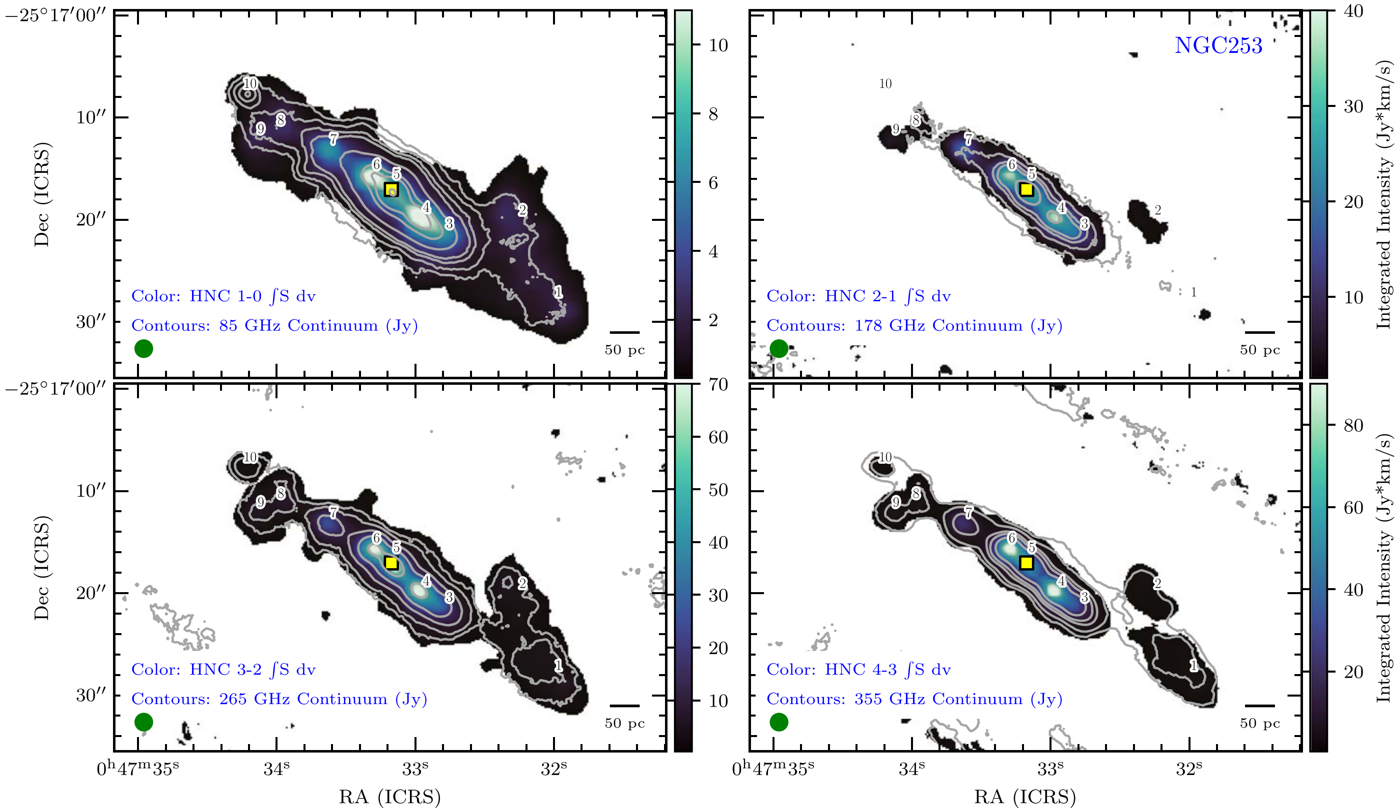

Figure 4. HNC integrated intensity (moment-0) images toward NGC 253. Markings, intensity scaling, and contours in each panel are the same as in Figure 3.

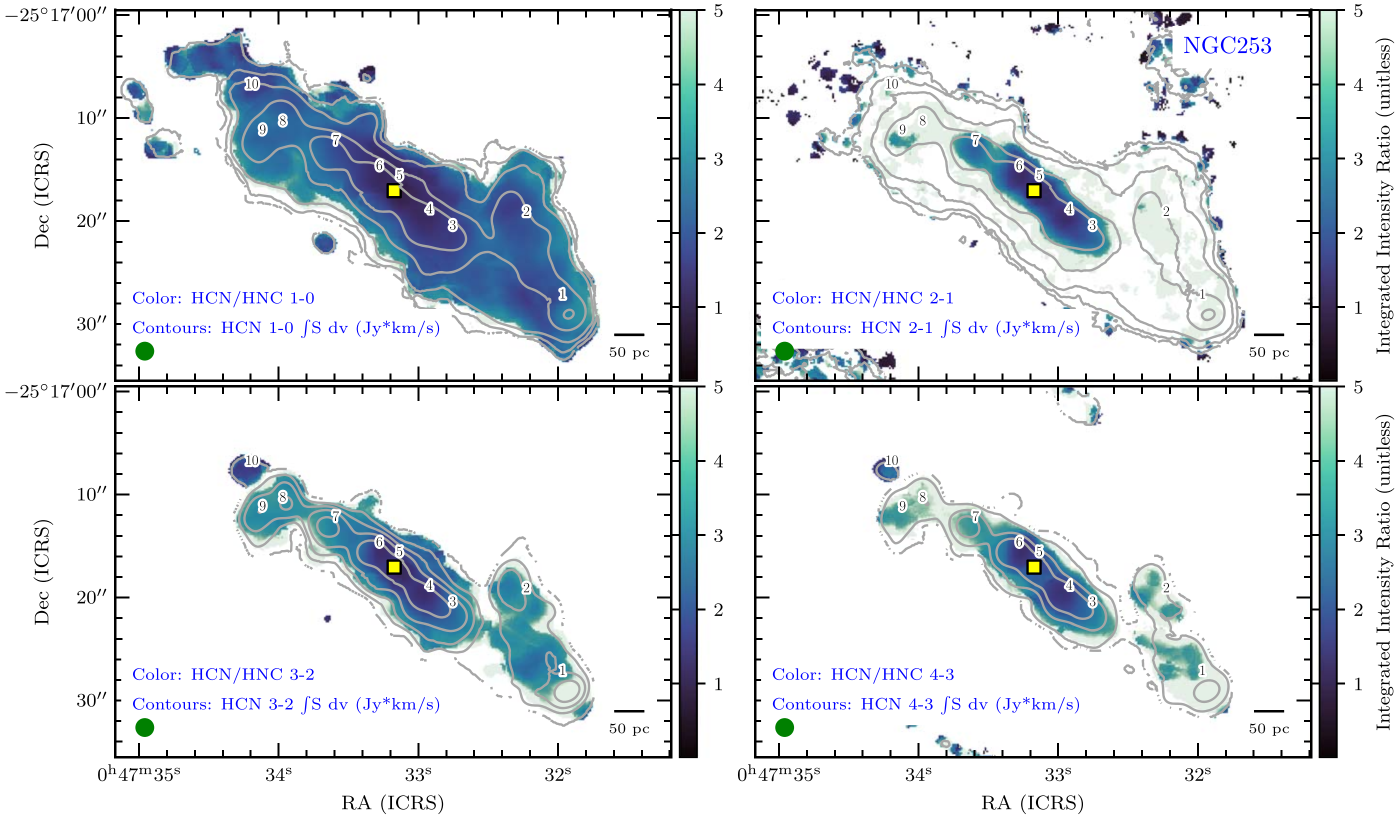

Figure 5. HCN/HNC integrated intensity (moment-0) ratio images toward NGC 253. Contour levels are (0.2, 0.5, 1.0, 3.0, 7.0), (1.0, 2.0, 4.0, 10.0, 20.0), (1.0, 5.0, 10.0, 20.0, 50.0), and (1.0, 5.0, 20.0, 50.0) Jy beam^{-1} km s^{-1} for the 1–0, 2–1, 3–2, and 4–3 HCN integrated intensities, respectively. Markings in each panel are the same as in Figure 3.

Table 2
GMC-averaged Integrated Intensities[a]

GMC	HCN 1–0	HCN 2–1	HCN 3–2	HCN 4–3	HNC 1–0	HNC 2–1	HNC 3–2	HNC 4–3
1	3.81(0.57)	12.86(1.95)	15.29(2.29)	14.93(2.24)	1.72(0.26)	0.53(0.57)	3.82(0.58)	2.45(0.40)
2	4.23(0.63)	13.43(2.03)	11.30(1.70)	8.56(1.23)	2.22(0.33)	2.04(0.64)	3.35(0.51)	1.71(0.30)
3	10.57(1.59)	35.16(5.28)	53.35(8.00)	62.51(9.34)	6.68(1.00)	17.04(2.62)	25.35(3.80)	26.98(4.05)
4	13.27(1.99)	49.11(7.37)	88.06(13.21)	116.47(17.47)	10.48(1.57)	34.04(5.14)	63.52(9.53)	77.60(11.64)
5	9.16(1.37)	45.41(6.82)	75.94(11.39)	99.24(14.89)	8.05(1.21)	28.63(4.33)	53.41(8.01)	48.47(7.27)
6	12.68(1.90)	49.86(7.49)	93.05(13.96)	123.40(18.51)	9.84(1.48)	31.92(4.82)	58.76(8.81)	73.21(10.98)
7	11.91(1.79)	42.65(6.40)	67.05(10.06)	74.06(11.11)	5.90(0.89)	16.98(2.61)	22.78(3.42)	19.91(2.99)
8	5.37(0.81)	15.52(2.35)	16.36(2.45)	13.00(1.95)	2.32(0.35)	2.77(0.70)	5.08(0.77)	3.05(0.48)
9	4.74(0.71)	14.53(2.20)	16.34(2.45)	14.10(2.12)	2.05(0.31)	4.01(0.82)	5.41(0.82)	3.90(0.61)
10	1.48(0.22)	3.74(0.63)	2.78(0.42)	1.93(0.31)	0.76(0.11)	0.58(0.57)	1.65(0.26)	0.85(0.20)

Note.

[a] All integrated intensities have units of jansky per kilometer per second with 1σ uncertainties shown within parentheses.

(This table is available in its entirety in machine-readable form.)

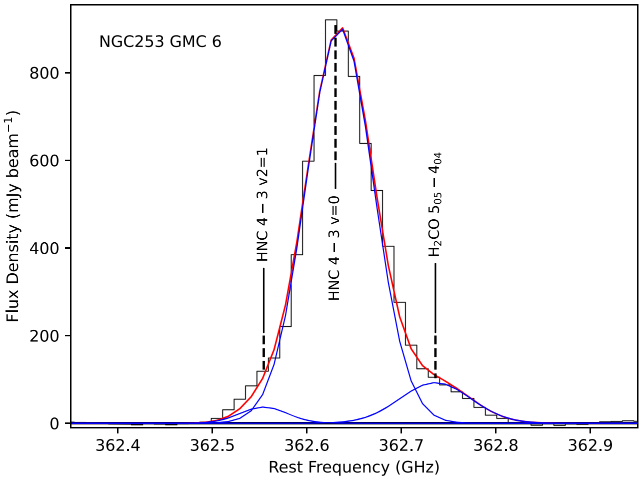

Figure 6. Spectral interloper diagnostic spectrum associated with HNC 4–3. Individual (blue lines) and cumulative (red lines) Gaussian fits are shown.

abundance at the source of the emission by our H_2 column density (Dyson & Williams 1997).

To incorporate radiative transfer modeling, we use `SpectralRadex`, a python library that includes a wrapper for the `RADEX`[25] (van der Tak et al. 2007) program. `RADEX` is a 1D non-LTE statistical equilibrium radiative transfer code that assumes an isothermal and homogeneous environment. Optical depth effects are treated within `RADEX` using an escape probability method. `RADEX` allows the user to do radiative transfer calculations while constraining physical conditions such as density and temperature. Given `UCLCHEM` chemical abundances and user-defined temperature, density, and H_2 column density values, we can use `RADEX` to connect chemical abundances to integrated intensities through the molecular column densities. We can then directly compare the model-predicted integrated intensities to our measurements. These integrated intensities are calculated assuming a uniform line width of 100 km s^{-1}, which is consistent with the line widths derived from our spectral line extraction procedure (Section 3.2) and a beam-filling factor of 1. It is also important to note that we only consider excitation through collisions with H_2 and therefore ignore electron collisions. A previous ALCHEMI-based study (Holdship et al. 2022) found that even at the CRIRs, which will be discussed later in this article (Section 4.4), almost all hydrogen is in its molecular form under these conditions. Holdship et al. (2022) found that toward GMCs 3–7 that the fractional abundance of electrons is in the range X (e^{-1}) ~ 10^{-4}–10^{-5} for volume densities $n(H_2) \lesssim 10^{5.5}$ cm^{-3}. Goldsmith & Kauffmann (2017) note that electrons could be of practical importance for HCN excitation when $n(H_2) < 10^{5.5}$ cm^{-3} and $X(e^{-1}) > 10^{-5}$. Even though electron-induced collisions could be important in the lower-density regions within the NGC 253 CMZ, we have opted to not consider electron-induced collisions in our analysis, and to defer further analysis of the potential impact of electron collisions in our model to future analysis.

As noted by Aalto et al. (2007b) the ground state vibrational energy levels of the HCN and HNC isomers can be populated via infrared excitation of the lowest-energy vibrational energy levels. This mechanism involves absorption of infrared photons by coupling to the lowest-energy ($v_2 = 1$) degenerate vibrational bending mode of each isomer. As described by Aalto et al. (2007b), this infrared coupling has the effect of exciting the ground vibrational states of the HCN and HNC isomers to higher rotational levels via a $\Delta J = 2$ selection rule. The $v_2 = 1$ bending modes in HCN and HNC have wavelengths of 14 and 22 μm (714 and 464 cm^{-1}, respectively), while their energies above ground (E_{IR}) are 1027 and 669 K, respectively. The Einstein-A coefficients for these vibrational bending modes are $A_{IR} = 1.7$ and 5.2 s^{-1} for HCN and HNC, respectively. Since the rate of an infrared pumped vibrational transition is given by $P_{IR} \propto A_{IR} / \exp(E_{IR} / T_{IR})$, where T_{IR} is the infrared brightness temperature, the HNC infrared pump is approximately two orders of magnitude faster than that for HCN. This difference in infrared pumping efficiency results in an HCN/HNC ground vibrational state spectral line intensity ratio that is less than 1. Since we do not measure spectral line intensity ratios less than 1 toward the NGC 253 CMZ (Section 3.2), we did not see a justification for including infrared excitation in our radiative transfer model. This does not mean that infrared excitation of the ground vibrational energy states of HCN and HNC do not exist in the NGC 253 CMZ, but that it is not a necessary excitation mechanism to explain our observations.

4.2. *Defining Bayesian Priors*

We are interested in estimating density, temperature, CRIR, and molecular hydrogen column density in the NGC 253 CMZ.

---

[25] https://home.strw.leidenuniv.nl/~moldata/radex.html

Table 3
Prior Distributions

	Parameter	Range	Distribution Type
T	Temperature	50–300 K	Uniform
n	Volume density	10^3–10^7 cm^{-3}	Log-uniform
ζ	CRIR	10–10^7 ζ_0[a]	Log-uniform
N_{H_2}	H_2 column density	10^{22}–10^{25} cm^{-2}	Log-uniform

Note.
[a] $\zeta_0 = 1.36 \times 10^{-17}$ s^{-1}.

Table 4
NGC 253 GMC Physical Parameters[a]

GMC	T_K (K)	$\log_{10}$ n (cm^{-3})	$\log_{10} \zeta$ (ζ_0)	$\log_{10}$ N_{H_2} (cm^{-2})
1	$172.53^{+75.77}_{-67.79}$	$3.81^{+0.90}_{-0.48}$	$3.87^{+0.15}_{-0.22}$	$22.85^{+0.82}_{-0.54}$
2	$135.94^{+69.52}_{-52.60}$	$3.89^{+0.85}_{-0.53}$	$3.80^{+0.20}_{-0.07}$	<23.79
3	$161.72^{+93.81}_{-65.15}$	$4.73^{+0.73}_{-0.88}$	$4.08^{+0.81}_{-0.24}$	$23.24^{+0.80}_{-0.79}$
4	NC	$5.31^{+0.48}_{-1.00}$	$4.82^{+0.79}_{-0.87}$	NC
5	NC	$5.62^{+0.31}_{-0.34}$	$5.09^{+0.39}_{-0.50}$	$23.50^{+0.87}_{-0.67}$
6	NC	$5.43^{+0.39}_{-0.81}$	$4.85^{+0.61}_{-0.86}$	$23.41^{+1.07}_{-0.86}$
7	$148.13^{+98.79}_{-60.97}$	$4.79^{+0.68}_{-0.97}$	$3.97^{+0.41}_{-0.16}$	<23.90
8	$162.11^{+80.99}_{-68.79}$	$3.92^{+0.68}_{-0.53}$	$3.90^{+0.14}_{-0.28}$	<23.86
9	$163.92^{+77.62}_{-62.81}$	$3.98^{+0.89}_{-0.58}$	$3.90^{+0.16}_{-0.16}$	<23.79
10	NC	$3.93^{+0.77}_{-0.58}$	$4.15^{+0.41}_{-0.46}$	<23.93

Note.
[a] Most likely parameters describing each GMC as a result of `UCLCHEM` + `RADEX` modeling and `UltraNest` sampling. Uncertainties indicate ±33% of the posterior distribution. <indicates upper limit (83rd percentile) of distribution. NC = not constrained.

Our choices for parameter prior distributions are listed in Table 3 for volume density n, kinetic temperature T, CRIR ζ, and molecular hydrogen column density N_{H_2}. For our temperature parameter, we sample kinetic temperatures between 50 and 300 K, adopting a flat prior distribution to uniformly sample the parameter space without bias. This kinetic temperature prior is based on the results of the Mangum et al. (2019) kinetic temperature measurements toward the NGC 253 CMZ. On the largest angular scales (~5″), Mangum et al. (2019) measured kinetic temperatures ~50 K. On smaller scales ($\lesssim$1″), Mangum et al. (2019) measured kinetic temperatures of at least 300 K.

We model CRIRs with a log-uniform distribution ranging from 10 ζ_0 to 10^7 ζ_0 (~10^{-16}–10^{-10} s^{-1}). We adopt this upper limit by taking into consideration estimates made by Holdship et al. (2021) and Harada et al. (2021), which derive ζ ranges from 10^3–10^6 ζ_0. Since Harada et al. (2021) estimate one general CRIR in the CMZ and Holdship et al. (2021) only analyze GMCs 3–7, we have no point of reference for outer GMCs 1, 2, 8, 9, and 10. Thus, we adopt a lower limit of 10 ζ_0 to account for a potentially low CRIR in these less active regions.

We adopt a log-uniform distribution for densities over the range of 10^3-10^7 cm^{-3}. Observations suggest gas densities of 10^5-10^6 cm^{-3} (Leroy et al. 2018; Harada et al. 2021), so we model densities centered on this range with a few orders of magnitude as a buffer both higher and lower than this estimate.

For our molecular hydrogen column density prior, we rely upon previous measurements of this quantity toward the CMZ of NGC 253. Millimeter dust continuum measurements over similar spatial scales as those modeled here were used to derive N_{H_2} in the range of 10^{23} to 7×10^{24} cm^{-2} for GMCs 3–7 (Mangum et al. 2019). From these measurements, we set the upper bound of our N_{H_2} prior to 10^{25} cm^{-2}. Since the Mangum et al. (2019) measurements did not sample GMCs 1, 2, 8, 9, or 10, which appear to be in regions of lower dust column density (Figure 1), we have adopted 10^{22} cm^{-2} for the lower-bound of our N(H_2) prior. Again, we use a log-uniform distribution for this prior.

4.3. Nested Sampling

We sample our parameter space to obtain input for our chemical models using nested sampling techniques by implementing the Monte Carlo algorithm MLFriends (Buchner 2016, 2019) using the `UltraNest`[26] package (Buchner 2021). `UltraNest`'s MLFriends algorithm estimates the posterior probability distribution of some parameters given our data, using Bayes' theorem

$$P(\boldsymbol{\theta}|\boldsymbol{F}_{\rm d}) = \frac{P(\boldsymbol{F}_{\rm d}|\boldsymbol{\theta})P(\boldsymbol{\theta})}{P(\boldsymbol{F}_{\rm d})}, \tag{3}$$

where $P(\boldsymbol{F}_{\rm d}|\boldsymbol{\theta})$ is the probability of obtaining some data F_d given a set of parameters θ (e.g., T, n), $P(\boldsymbol{\theta})$ is the prior probability of those parameters, and $P(\boldsymbol{F}_{\rm d})$ is the Bayesian evidence.

We can determine $P(\boldsymbol{F}_{\rm d}|\boldsymbol{\theta})$ by assuming Gaussian errors giving the standard function

$$P(\boldsymbol{F}_{\rm d}|\boldsymbol{\theta}) = \exp\left(-\frac{1}{2}\sum_i \frac{(F_{d,i} - F_{t,i})^2}{\sigma^2_{F,i}}\right). \tag{4}$$

In Equation (4), we compare our data F_d and its uncertainty σ_F to the output of our forward model F_t for any given set of parameters that we obtain for each transition i.

To sample the posterior distribution, `UltraNest` initially samples the entire parameter space by selecting a number of parameter combinations, called "live points", based on the prior probability of our parameters, and then replacing the least likely of these combinations based on the results from chemical and radiative transfer modeling. As shown graphically in Figure 7, in each iteration, the selected parameters are fed into `UCLCHEM`, producing chemical abundances of the desired HCN and HNC transitions as a fraction of total H nuclei. We combine modeled abundances with molecular hydrogen column density as a free parameter to obtain HCN and HNC column densities. We input these values into `SpectralRadex` to obtain integrated intensities to compare to our ALMA observations of the HCN and HNC 1–0, 2–1, 3–2, and 4–3 transitions. `SpectralRadex` produces integrated intensities in Kelvin times kilometers per second, so we can use the following equation to convert our observed beam-averaged integrated intensities from jansky to Kelvin times kilometers per second

$$T_R({\rm K}) = 13.59\left(\frac{300{\rm GHz}}{\nu}\right)^2 \times \left(\frac{1''}{\theta_{\rm max}}\right)\left(\frac{1''}{\theta_{\rm min}}\right) I({\rm Jy}), \tag{5}$$

---

[26] https://johannesbuchner.github.io/UltraNest/

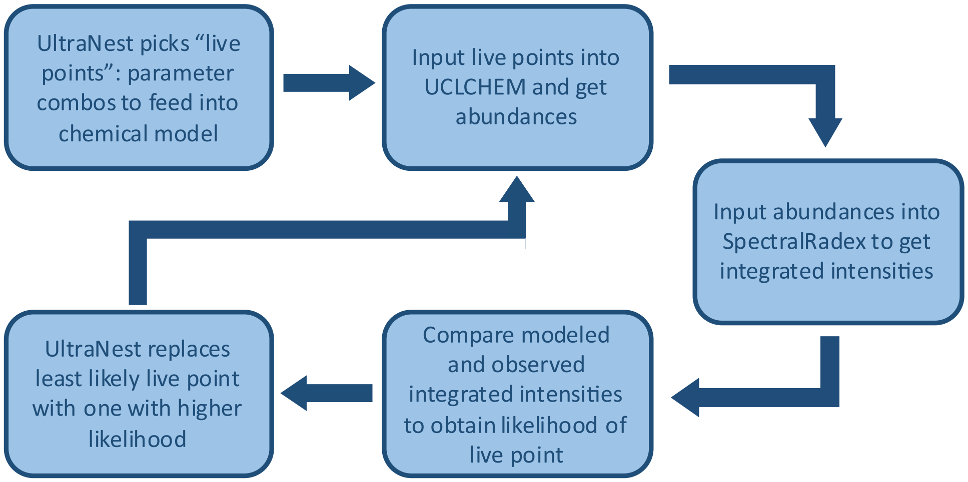

Figure 7. Flowchart describing our nested sampling + chemical and radiative transfer modeling process.

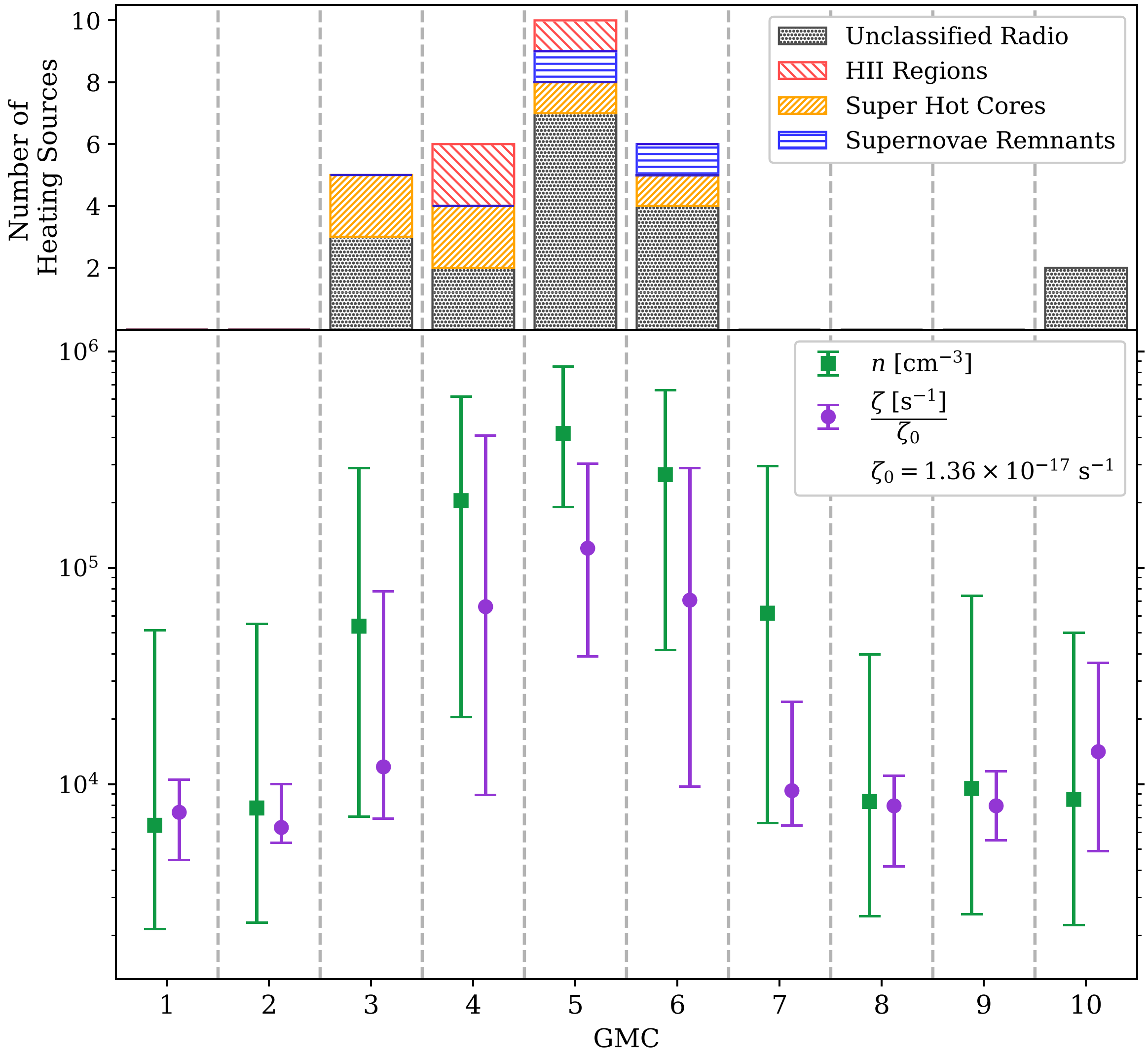

Figure 8. Top: number of heating sources per GMC. Unclassified, supernovae remnants, and H II regions are from Ulvestad & Antonucci (1997), while super hot cores are from Rico-Villas et al. (2020). Note that the super hot core source measurements sample only the inner portion of the NGC 253 CMZ, which includes GMCs 3–6. Bottom: median modeled volume density (green squares) and CRIR (purple circles) values for each GMC. Error bars indicate the 16th–84th percentile of the posterior distributions.

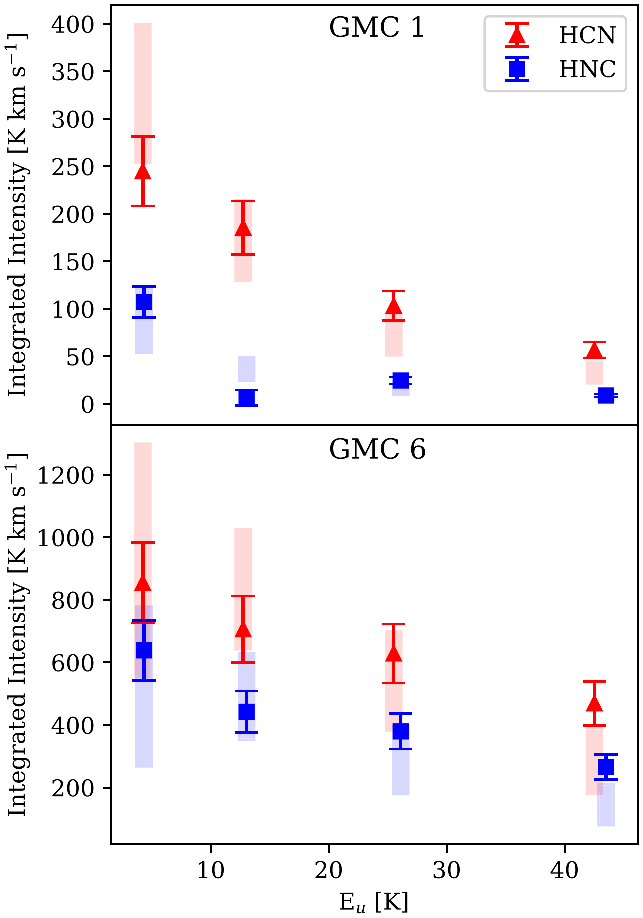

Figure 9. Observed (triangles and squares) vs. modeled (shaded bars) flux for HCN (red) and HNC (blue). Observed error bars indicate the 1σ uncertainty range. Shaded rectangles show the inner 67% (∼16th–84th percentile) of our modeled flux distributions.

where ν is the rest frequency of the line, $\theta_{\rm max}$ and $\theta_{\rm min}$ are the FWHMs of the major and minor axes of our Gaussian beam, and I is our integrated intensity. In our case, $\theta_{\rm max} = \theta_{\rm min} = 1\farcs6$. At each iteration, the live point with the lowest likelihood is removed and replaced with a more suitable point, which results in the volume of the sampled parameter space shrinking. These iterations continue until the live point weights are insignificant (fractional remainder $\leqslant$0.01), indicating the vast majority of the probability density has been sampled.

4.4. Modeling Results

The most likely physical parameters for each GMC as a result of our modeling and sampling algorithms are shown in Table 4 and Figure 8 and are compared in the latter to the number of heating sources per GMC. We show results using the high-temperature barriers (2000, 1200 K) for the HNC + O and HNC + H reactions, as we find varying the temperature barrier had no discernible effect on our results. A possible explanation for this result is presented in Section 4.5. The most likely parameters found using each of the two temperature barriers were well within the error bars of the opposing model's parameter estimates. In Table 4, we report the median values of the posterior distributions for each parameter with uncertainties that represent the inner 67% of the distributions. We find that kinetic temperature and H_2 column density are largely not constrained by our HCN and HNC measurements. Nearly all values of kinetic temperature and H_2 column density have an equal likelihood of describing our data, rather than a concentration of points with a high likelihood of existing in a small fraction of the parameter space. In cases where the posterior distributions peak at the lower end of our parameter space, we instead report the 83rd percentile of the distribution as an upper limit in Table 4. However, we are able to constrain volume density and CRIR, finding $n \sim 10^4$–$10^{5.5}$ cm^{-3} and $\zeta \sim 10^{-13}$–10^{-12} s^{-1} across the GMCs. Our inability to constrain $T_{\rm K}$ and $N_{\rm H_2}$ is discussed further in Section 4.5.

We see a bimodality in the CRIR marginalized posterior distributions with solutions at $\sim 10^4\,\zeta_0$ and $\sim 10\,\zeta_0$ (see Figures 10 and 11). We investigated the cause of this bimodality by comparing our model outputs to the data when sampling parameters from each mode. We expected that the low CRIR solution would favor one species or a subset of the transitions, while the high CRIR solution would favor another. However, we find no such physical connection between the low-ζ solutions and any subset of species or transitions. We suggest that the most likely scenario that can explain the low-ζ solution is that the part of the parameter space corresponding to low-ζ values simply happens to produce integrated intensities somewhat close to our measured values. Strong evidence from previous studies based on other sets of molecular lines observed in ALCHEMI (Harada et al. 2021; Holdship et al. 2021, 2022) indicates that the CRIR in the inner GMCs, some of which show bimodality in our models, is $>10^3\zeta_0$. As such, we dismiss the lower CRIR solution across all GMCs as unphysical and only present the high CRIR solutions.

To show examples of results for GMCs both in the outer and inner parts of the CMZ, the observed and modeled fluxes for GMCs 1 and 6 are shown in Figure 9. Observed and modeled fluxes for the remaining GMCs can be found in Appendix B. Figures 10 and 11 show corner plots for GMCs 1 and 6, respectively, demonstrating our results and the relationships between physical parameters. Corner plots for GMCs 2–5 and 7–10 can be found in Appendix B. Our results show an enhancement in volume density and CRIR in the central GMCs (4–6) versus the outer GMCs. One explanation for this increase in volume density and CRIR could be a degeneracy between these two quantities. In Figure 11, the panel showing the relationship between n and ζ does demonstrate that as n increases by ∼2.5 dex ζ increases by ∼1 dex. If n and ζ were degenerate, we would expect to see an equal change in the spread for both parameters across all GMCs. Thus, we believe the behavior demonstrated in Figure 8 is a physical solution rather than resulting from a degeneracy.

Figure 12 shows a violin plot displaying the HCN/HNC abundance ratios from the best-fitting 67% of models for all GMCs, where the distribution of values is consistent with the signal-to-noise (S/N) levels in each GMC. GMCs in the center of the nucleus have a higher S/N and exhibit a smaller spread of values when compared to the outer GMCs. We also see that the modeled HCN/HNC abundance ratio is lower in GMCs with higher CRIRs (Figure 13). In order to determine the significance of this apparent anticorrelation, we calculate the Spearman coefficient ρ for the relationship between CRIR and the HCN/HNC abundance ratio by employing the `SciPy` (Virtanen et al. 2020) function `spearmanr`[27] (Kokoska & Zwillinger 1999).

---

[27] https://docs.scipy.org/doc/scipy/reference/generated/scipy.stats.spearmanr.html

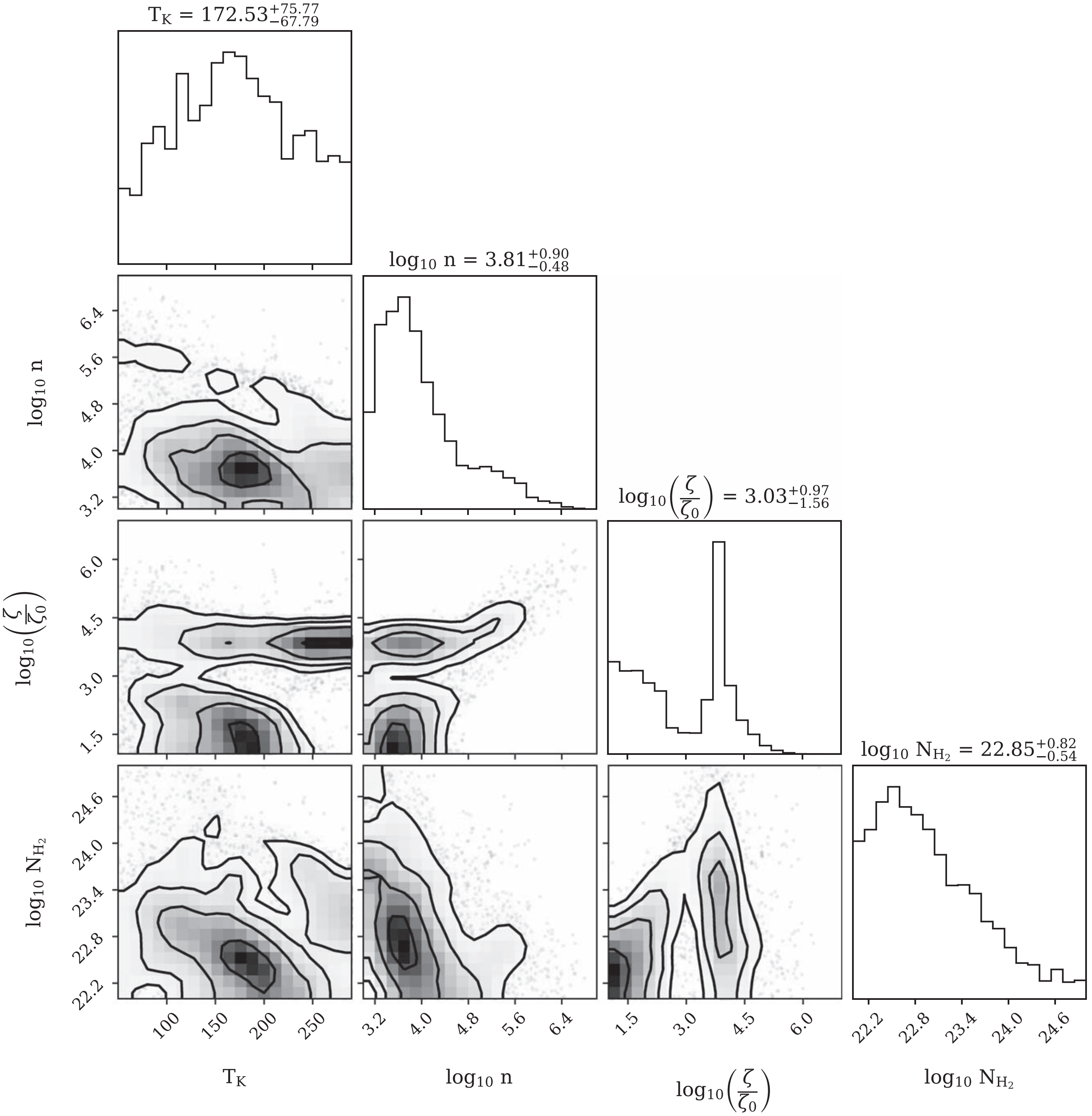

Figure 10. Modeling results for GMC 1.

We use our modeled abundance ratios and CRIR estimates for each GMC in combination with their uncertainties to create simulated Gaussian data sets for these parameters consisting of 10,000 sets of 10 data points each (1 point for each GMC).[28] We calculate ρ for each set of 10 data points in the simulated distributions and find that the median ρ value is -0.47 ± 0.26 (Figure 13). This ρ value indicates there is a moderately anticorrelated relationship between CRIR and the HCN/HNC abundance ratio.

We find that we are able to reproduce our measured integrated intensity ratios using cosmic-ray ionization applied through `UCLCHEM` gas-grain chemical modeling. Furthermore, the HCN/HNC integrated intensity and abundance ratios are far less than ∼50, which was suggested by Meijerink et al. (2011) for cases of significant mechanical heating. Thus, our results place NGC 253 in the regime of low mechanical heating and high CRIR, which can be seen in Figure 2 for the case of no mechanical heating. The HCN and HNC chemistry that results in these low ratios is discussed in Section 4.5. Our observed integrated intensity ratios are consistent with other extragalactic HCN and HNC measurements (Section 2), suggesting that these galaxies belong to the same part of the heating parameter space as NGC 253.

Even though our `RADEX` radiative transfer model accounts for optical depth, there may be a concern that very high optical depths in our HCN and HNC transitions might influence our modeling results. To this end, we used our `RADEX` analysis to estimate the optical depth of our HCN and HNC transitions.

---

[28] https://www.jonathan-liu.com/post/correlationanalysismontecarlo/

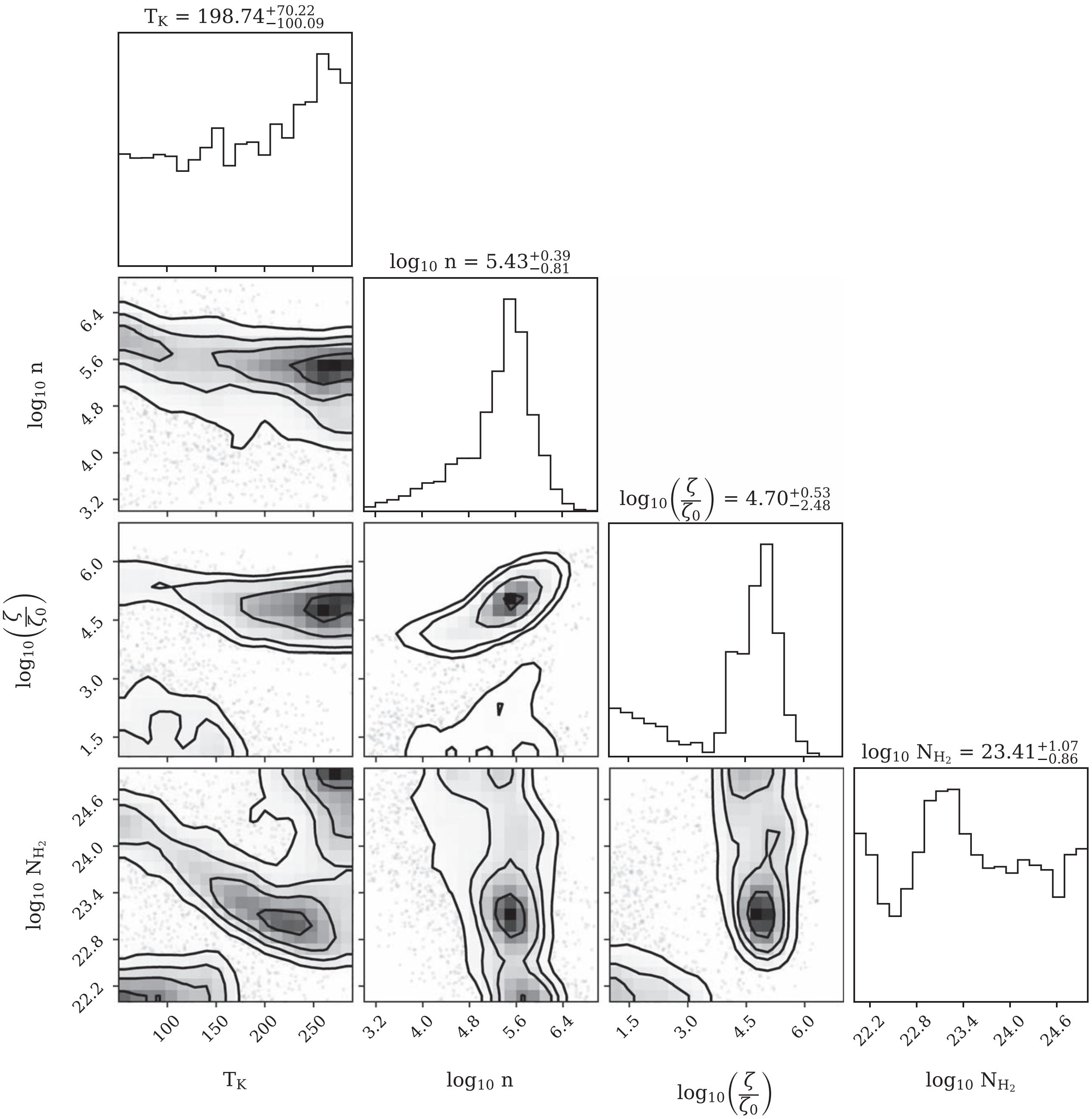

Figure 11. Modeling results for GMC 6.

We model the optical depth for all iterations of our `UltraNest` sampling algorithm and analyze the middle 67% of the resulting distribution. We find that overall, the optical depth distributions peak at reasonably low ($\lesssim$10) values. We measure slightly higher optical depths in the HCN 1–0 and 2–1 transitions, but the optical depths in the corresponding HNC transitions toward all GMCs are similar. The modeled optical depth values across HCN and HNC for all transitions are also close enough in value that we rule out the possibility that different transitions are tracing different physical structures. To confirm these optical depth estimates, we use integrated intensity isotopic ratios for HCN/H^{13}CN and HCN/HC^{15}N (Martín et al. 2019), as well as their isotopomers, to modify our HCN and HNC abundance values from `UCLCHEM` and thus model the optical depth of these isotopic variants. We found that the ratios of modeled optical depths are consistent with the observationally derived isotope ratios themselves, confirming that our modeled optical depths are consistent with observations. Additionally, since we model all of the HCN and HNC transitions together, we are effectively deriving an average set of physical parameters across those regions probed by these HCN and HNC transitions. Thus, we conclude that optical depth issues do not inhibit the use of our observed integrated intensities in constraining our models.

4.5. Effect of Cosmic Rays on the HCN/HNC Ratio

Our results show that the observed HCN/HNC integrated intensity ratios in the NGC 253 CMZ can be replicated through CRIRs several orders of magnitude higher than those found

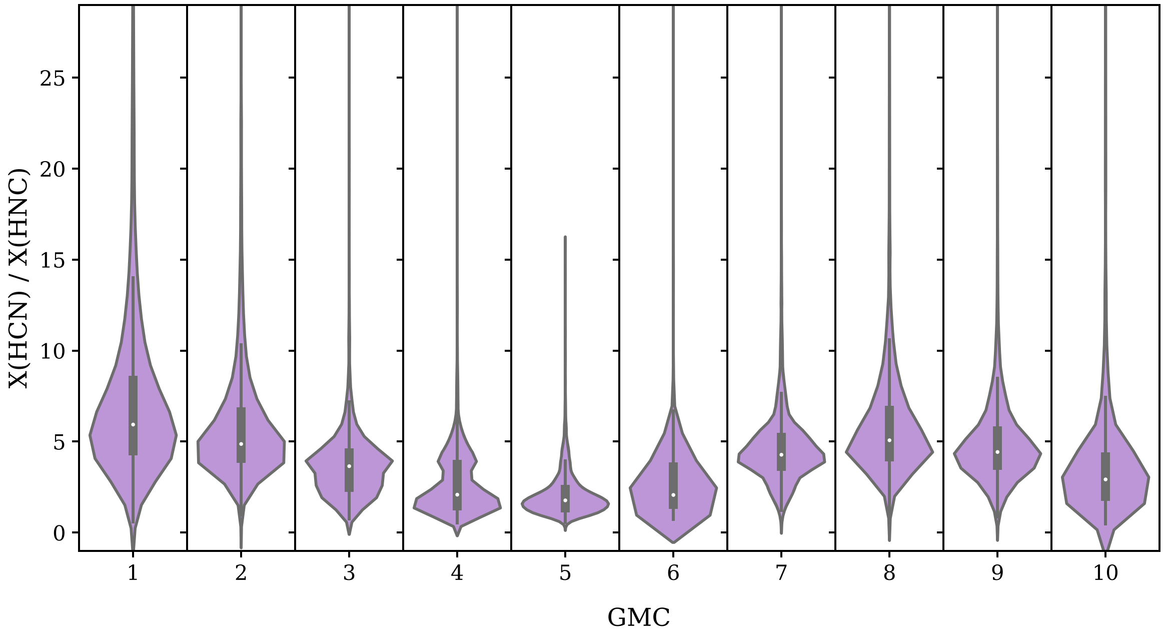

Figure 12. Violin plots derived from modeled HCN/HNC abundance ratios for all GMCs using the most likely 67% of models. Purple violins indicate the smoothed kernel density estimations of the ratio distributions for each GMC. White dots at the center of each violin indicate the median values of the HCN/HNC ratios derived from `UCLCHEM`'s abundance estimates. The thick gray vertical bars within each violin show the interquartile ranges of the `UCLCHEM` data sets, and the thin gray lines illustrate the two outer quartiles.

locally in our own Galaxy. Since `UCLCHEM`'s treatment of cosmic rays artificially separates cosmic-ray ionization from cosmic-ray heating, we estimate the heating that would result from these CRIRs via the photon-dominated region (PDR) modeling code `UCLPDR`[29], which treats heating and cooling. `UCLPDR` provides an estimated gas temperature given input volume densities and CRIRs, assuming an $A_V \sim 10$ (in this case in order to model the inner, UV-shielded part of the cloud). We see in Figure 14 that the density and CRIR estimates in the inner GMCs (4–6) result in PDR gas temperatures of ~200–500 K, whereas the conditions in the outer GMCs correspond to temperatures of ~100–400 K. We can assume that if these PDR-derived temperatures were lower than those calculated from observations, the additional heating needed to equate the temperatures would be from mechanical heating. However, the high kinetic temperatures from our PDR modeling agree with those derived by Mangum et al. (2019) and overlap with the kinetic temperatures found through `UCLCHEM` modeling, when constrained. Thus, we conclude that there is little contribution from mechanical heating and that cosmic-ray heating alone can produce high kinetic temperatures.

Previous studies (e.g., Goldsmith et al. 1986; Herbst et al. 2000; Meijerink et al. 2011; Kazandjian et al. 2012; Krieger et al. 2020) have suggested that the HCN/HNC abundance ratio might probe mechanical heating processes in the ISM through its kinetic temperature sensitivity, with the ratio increasing at high kinetic temperatures. This behavior has been seen in observations of protostellar shocks (e.g., Lefloch et al. 2021) and C-type shock models, where the HCN/HNC abundance ratio increases by a factor of ~20. Hence, we would expect that mechanical heating by shocks in NGC 253 would produce high HCN/HNC abundance ratios (Viti 2017). Given that we do not observe high ratios in NGC 253, it appears that shocks are not a dominant source of heating. However, as noted above via PDR modeling, our high CRIRs are still capable of raising the gas temperature, so we must explain how we observe low HCN/HNC ratios while still measuring a high temperature (Mangum et al. 2019). We therefore investigate the detailed chemical network used by our model and find that identical temperature-independent formation and destruction routes dominate the chemistry of HCN and HNC at high CRIR.

To see how these chemical pathways drive the HCN and HNC abundance as the CRIR is increased, we start at a low CRIR. The primary source of HCN at low CRIR varies with temperature but is usually a reaction with a small barrier, e.g.,

$$\begin{aligned}
&\mathrm{H_2 + CN \longrightarrow HCN + H\ (E_A = 250\ K)}\\
&\mathrm{N + HCO \longrightarrow HCN + O\ (E_A = 50\ K)}\\
&\mathrm{N + CH_2 \longrightarrow HCN + H\ (E_A = 50\ K),}
\end{aligned}$$

where E_A is the energy barrier in Kelvin. Routes to form HNC are much less efficient, such that one would expect the HCN/HNC abundance ratio to increase with temperature at low CRIR due to the increasing efficiency of HCN formation. This result is consistent with the finding of Meijerink et al. (2011, Figure 2), demonstrating that the HCN/HNC abundance ratio is sensitive to and positively correlated with the kinetic temperature at low CRIR.

However, at a sufficiently high CRIR, this picture changes. Both species then form mainly through the reactions

$$\begin{aligned}
&\mathrm{HCNH^+ + e^- \longrightarrow HCN + H}\\
&\mathrm{HCNH^+ + e^- \longrightarrow HNC + H,}
\end{aligned}$$

which have identical rates at all temperatures. Once the CRIR is large enough for these reactions to dominate, both species form at roughly identical rates. Kinetic temperature is no longer as much of an issue, leading to a convergence toward low HCN/

---

[29] https://uclchem.github.io/ucl_pdr/

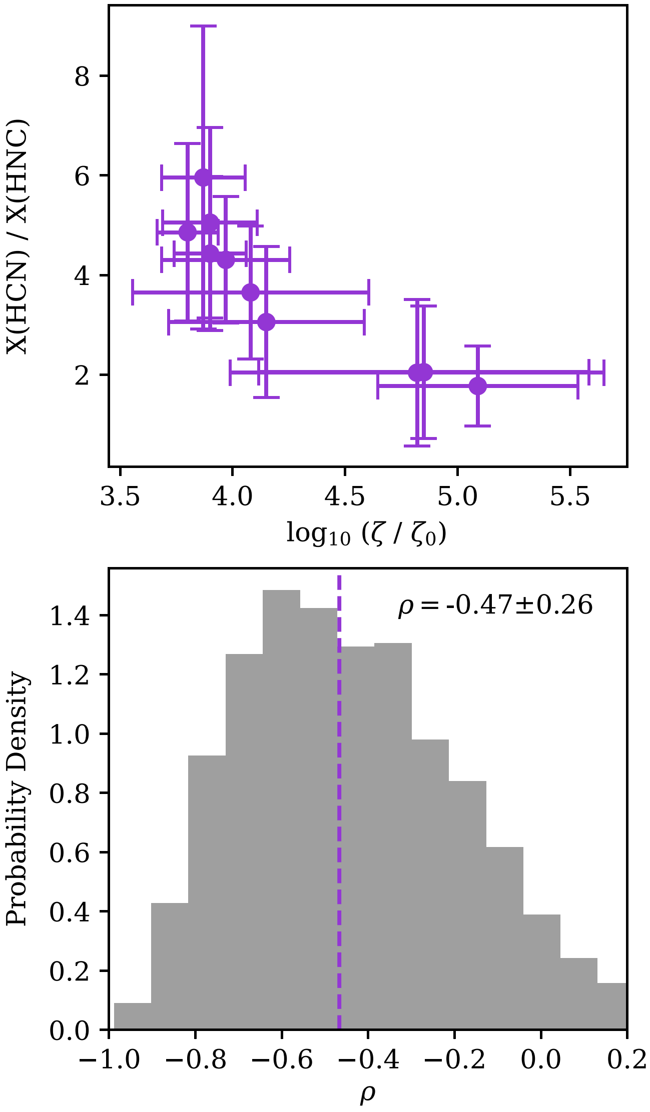

Figure 13. Top: HCN/HNC abundance ratio as a function of CRIR. Bottom: distribution of Spearman coefficients for a simulated Gaussian data set derived from our modeled HCN/HNC abundance ratios, CRIRs, and their uncertainties. The given value of ρ represents the median of the distribution.

HNC abundance ratios across all mechanical heating rates as seen in Figure 2.

The destruction pathways for HCN and HNC are much simpler. Regardless of CRIR, both species are primarily destroyed by reactions with ions. At high CRIR, these proceed much faster because there are more ions but there is no real change of destruction route. In the end, then, the HCN/HNC abundance ratio is largely set by relative formation efficiency rather than destruction. As a result, at high CRIRs, HCN, and HNC chemistry is dominated by cosmic rays rather than kinetic temperature. Because NGC 253 seems to fall in this high end of the CRIR parameter space, our HCN and HNC observations toward NGC 253 allow us to constrain the CRIR but not kinetic temperature. Because there is a clear degeneracy between temperature and column density, which is demonstrated by the negative relationship shown in the N_{H_2} versus T_K corner plot panels in Figures 10 and 11, the inability to constrain kinetic temperature with our measurements also prevents us from constraining column density.

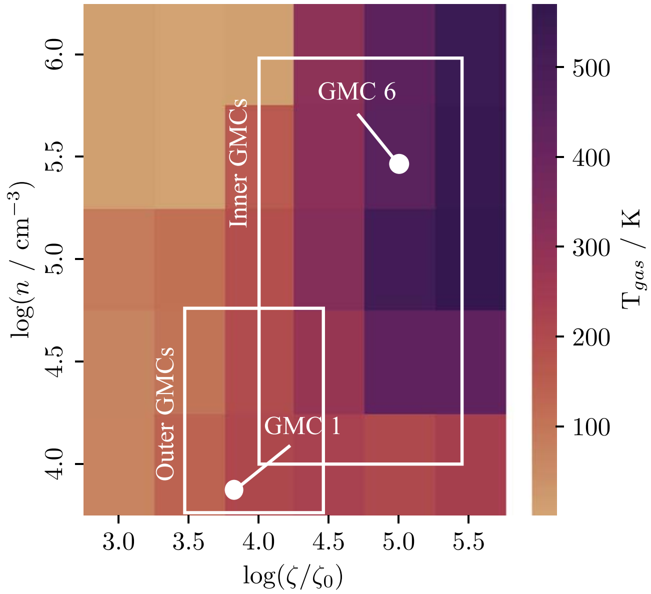

Figure 14. PDR modeling results from `UCLPDR` for gas temperature as a function of volume density and CRIR. White boxes indicate the areas of the plot relevant to the conditions in the outer and inner GMCs, and white dots note the specific locations of GMCs 1 and 6.

5. Discussion

5.1. Influence of Heating Sources

A result of our chemical and radiative transfer modeling (Section 4) of the GMCs in NGC 253 is an apparent volume density and CRIR gradient in the NGC 253 CMZ. Figure 8 shows that in GMCs 4–6, the predicted density and CRIR values are upward of an order of magnitude higher than in the outer GMCs. Our CRIR values agree with those found in other recent molecular studies of the NGC 253 CMZ. Holdship et al. (2021) determined that CRIRs of 10^3–$10^6\,\zeta_0$ ($\sim 10^{-14}$–10^{-11} s^{-1}) could replicate the C_2H emission seen in the CMZ. Additionally, Harada et al. (2021) used HOC^+ observations to estimate $\zeta \gtrsim 10^{-14}$ s^{-1}. Holdship et al. (2022) found that H_3O^+ and SO measurements corresponded to $\zeta \sim 10^{-13}$ s^{-1}, or $10^4\,\zeta_0$.

Volume density also appears to be enhanced in GMCs 4–6 compared to the outer GMCs. Our density estimates are consistent with those presented in Harada et al. (2021), who found $n_H \gtrsim 10^5$ cm^{-3} in molecular clumps and $n_H \sim 10^{4.5}$ cm^{-3} in more extended areas of the CMZ. We estimate slightly lower densities than Harada et al. (2021) in the outer GMCs, with $n \lesssim 10^4$ cm^{-3}. Leroy et al. (2015) suggest that the average volume density over the three-dimensional FWHM size of a GMC is $n_{H_2} \sim 2000$ cm^{-3} in these 10 GMCs, which is slightly lower than our estimates.

The highest densities and CRIRs, found in GMCs 4–6, are consistent with the density of heating sources present in these clouds. We place heating sources observed using radio continuum (Ulvestad & Antonucci 1997) and vibrationally excited HC_3N emission (Rico-Villas et al. 2020) in each of our 10 GMCs by simply identifying which sources fall within a GMC on the plane of the sky (i.e., no distance component is considered).

We examine the possible relationship between both density and CRIR and the number of heating sources per GMC by calculating Spearman coefficients for the CRIR-heating source and density-heating source relationships. Following the procedure we outlined in Section 4.4, we find that the median ρ values for the CRIR-heating source and density-heating source relationships are 0.67 and 0.60, respectively, with standard deviations of 0.21 and 0.17. These values indicate that there are likely positive correlations in the relationships between both CRIR and heating sources as well as density and heating sources. A higher volume density would lead to more favorable star-forming conditions, thus increasing the number of star formation-related heating sources. The increase in the number of heating sources will therefore increase the CRIR, as we expect these heating sources (e.g., supernova remnants) to be the main progenitor of cosmic rays.

The majority of heating sources (H II regions, supernova remnants, and super hot cores[30]) are located in the nucleus (GMC 5) of the CMZ (Figure 8), likely contributing to the enhanced CRIRs predicted there. Though many of these sources are unclassified, we estimate that approximately half of these unclassified sources are supernova remnants producing a high CRIR. This estimate is based on the analysis provided by Ulvestad & Antonucci (1997), who determined that $7/14$ ($\sigma_\alpha < 0.2$) and $8/17$ ($\sigma_\alpha < 0.4$) of the sources for which they derived spectral indices had $\alpha \leqslant -0.4$, indicative of synchrotron emission. Very few heating sources are found in outer GMCs 1, 2, and 8–10, which is consistent with our finding that the predicted CRIRs and densities are about an order of magnitude lower than in the nucleus. Furthermore, the sources of the cosmic rays appear to be well correlated with the prevalence of supernovae in the NGC 253 CMZ.

5.2. Connection between CRIR and Supernovae

In the interest of identifying a possible source for the cosmic rays traced by HCN and HNC chemistry in the NGC 253 CMZ, we seek to establish a connection between our measured CRIR and supernovae. In the ISM, the main effect of cosmic rays on ISM chemistry is to initiate and drive the interstellar chemistry by colliding with and ionizing atoms and molecules. During ionization they also transfer energy to the ejected electrons and hence heat the gas. While the energies of cosmic rays range from megaelectronvolt to ultrarelativistic values, the cosmic rays that are primarily responsible for ionizing the ISM are those with energies $\lesssim$1 GeV. Measuring the CRIR below such energies is often done by studying the products of ion-neutral chemistry in the dense ISM.

In our chemical models, $\zeta_0 = 1.36 \times 10^{-17}$ s^{-1} is used as the base CRIR from which all cosmic-ray-induced reactions are scaled. This model ζ_0 value appears to be similar to the local Milky Way CRIR. Analysis by Webber (1998) used data from the Voyager and Pioneer spacecraft at a distance of 60 au from the Sun to estimate the local interstellar cosmic-ray spectra and associated energy density and ionization rate lower limit. The energy density derived from this analysis is $\sim$1.80 eV cm^{-3}, while the implied CRIR lower limit is $\zeta_{\rm MW} \gtrsim (3 - 4) \times 10^{-17}$ s^{-1}, within a factor of 2 of the ζ_0 assumed in our chemical modeling. Uncertainties in the kinetic energy deposited into the gas per interaction alone (i.e., the energy produced by ionization of H_2 is 20 eV; Goldsmith 2001) are within this range of uncertainty.

It is also important to note that the CRIR in the Milky Way CMZ is measured to be $\sim$1000 times the local MW CRIR. Le Petit et al. (2016), using measurements of H_3^+, derive CRIRs in the range 1–11 $\times 10^{-14}$ s^{-1}, though this analysis found that this CRIR applies in a medium where the volume density n(H_2) $\lesssim$100 cm^{-3} to which the H_3^+ emission is sensitive. Ginsburg et al. (2016), using measurements of the H_2CO 3_{03}–2_{02} and $3_{21}-2_{20}$ transitions, derive an upper limit to the CRIR of $\lesssim 10^{-14}$ s^{-1} in the MW CMZ, constrained by their derived dense gas kinetic temperature of 60 K. The H_2CO transitions used in this analysis are sensitive to volume densities n_{H_2} $\sim 10^4$–10^5 cm^{-3}, similar to the volume densities probed by our HCN and HNC measurements. Ginsburg et al. (2016) concluded that CR heating is either not dominant in the MW CMZ or is not uniform.

As summarized by Dalgarno (2006), a lower limit to the Milky Way CRIR, $\zeta_{\rm MW}$, was established by Spitzer & Tomasko (1968) as $\gtrsim 6.7 \times 10^{-18}$ s^{-1} for hydrogen atoms. Also, based on a general consideration of energies released in supernovae, Spitzer & Tomasko (1968) estimated that the probable upper limit to $\zeta_{\rm MW}$ is 1.2×10^{-15} s^{-1}. This upper limit is obtained by assuming that the atoms in Type I supernova shells, which have an energy of 2 MeV per nucleon at a velocity of 20,000 km s^{-1}, permeate the Galaxy. If at most one-third of the shell energy of 10^{51} erg is available to the expanding shell of gas, with an energy loss of 36 eV per free electron produced during the ionization process, a galactic frequency of one Type I supernova per 100 yr gives the upper limit to $\zeta_{\rm MW}$ quoted.

These analyses suggest a quantitative connection between supernovae and the CRIR where a value for $\zeta_{\rm MW}$ of 1.2×10^{-15} s^{-1} corresponds roughly to a supernova rate of 0.01 yr^{-1}. Since our CRIR scaling constant is $\zeta_0 = 1.36 \times 10^{-17}$ s^{-1}, the CRIR represented by ζ_0 corresponds to a supernova rate of $\sim 10^{-4}$ yr^{-1}. The supernova rate for NGC 253 has been estimated to be in the range of 0.14–0.3 yr^{-1} (Ulvestad & Antonucci 1997; Lenc & Tingay 2006), and an upper limit to the supernova rate of 0.3 yr^{-1} would imply an upper limit to the CRIR of $\sim 3000\,\zeta_0$. This CRIR is on the low end of the range of ζ values that we measure toward the GMCs of NGC 253 (Figure 8). The distribution of radio sources with supernova-like spectral indices (Section 5.1) indicates a higher CRIR within GMCs associated with larger numbers of supernovae in NGC 253, consistent with the observed trend in CRIR within the CMZ (Figure 8).

6. Conclusions

We study HCN and HNC emission and its utility in investigating heating processes associated with star formation in the CMZ of the nearby starburst galaxy NGC 253. Previous studies suggested that the HCN/HNC line ratio would be useful in probing mechanical heating, which was thought to be an abundant heating source in the NGC 253 CMZ. However, our observations of low HCN/HNC integrated intensity ratios in combination with high kinetic temperatures indicate that either this ratio does not provide insight into the mechanical heating input or that mechanical heating is not a significant heating mechanism in this environment. To understand the implications of our observed integrated intensities, we model the physical conditions in the NGC 253 CMZ using chemical modeling via `UCLCHEM`and non-LTE radiative transfer modeling with `RADEX`. After constraining these models with our

---

[30] Keep in mind, though, that the measurements identifying super hot cores (Rico-Villas et al. 2020) sample only the part of the NGC 253 CMZ encompassing GMCs 3–6.

HCN and HNC measurements, we came to the following conclusions:

1. The HCN/HNC abundance ratios are low (<10) in the NGC 253 CMZ. This result is consistent with findings in other extragalactic systems but is at odds with previous theoretical work that suggested this ratio should be high ($\gtrsim 50$) in starburst galaxies with substantial mechanical heating (Meijerink et al. 2011; Kazandjian et al. 2012).
2. The HCN/HNC abundance ratios are lowest in GMCs with the highest modeled CRIRs and densities, and we find a moderate anticorrelation between the CRIR and the HCN/HNC ratio (Figure 13).
3. We see higher CRIRs in the center of the CMZ ($\zeta \sim 10^{-12}$ s^{-1}) as compared to those on its outskirts ($\zeta \sim 10^{-13}$ s^{-1}) (Figure 8).
4. Volume density is also enhanced in the central GMCs ($n_{H_2} \sim 10^{5.5}$ cm^{-3}) as compared to the outer GMCs ($n_{H_2} \lesssim 10^4$ cm^{-3}).
5. The central GMCs with the highest estimated density and CRIRs also contain the greatest number of heating sources (H II regions, supernova remnants, and super hot cores; Figure 8) per GMC, with statistical tests indicating a positive correlation between both of these parameters and the number of heating sources per GMC.
6. Our analysis suggests a quantitative connection between supernovae and the CRIR in NGC 253. With an estimated supernova rate in the range of 0.14–0.3 yr^{-1} (Ulvestad & Antonucci 1997; Lenc & Tingay 2006), an upper limit to the supernova rate of 0.3 yr^{-1} would imply an upper limit to the CRIR of $\sim 3000\ \zeta_0$. This CRIR is on the low end of the range of CRIRs that we measure toward the GMCs of NGC 253 (Figure 8).

Further work is needed to test the effectiveness of these molecular tracers on other star-forming environments, as different interpretations of the HCN/HNC abundance ratio are possible in cosmic ecosystems exhibiting different conditions. However, NGC 253 remains an excellent laboratory for studying extragalactic star formation due to its location in our proverbial backyard, and future studies will lay the groundwork for expanding the analysis to other galaxies. We hope to further unravel NGC 253's CMZ by combining tracers from other ALCHEMI studies in order to further constrain the CRIR, along with other key physical parameters. These data will aid in affirming the interpretations of various tracer molecules and will greatly enhance our understanding of star formation in a starburst environment.

We thank the anonymous referee for providing an extremely thorough and constructive review of the original version of this article. The referee's comments and suggestions resulted in numerous improvements to the research presented in this article, for which we are grateful. We thank Jack Warfield for his technical expertize in getting this project off the ground. We also thank Heihei Behrens for his crucial support to the authors throughout this process. This work is part of a project that has received funding from the European Research Council (ERC) under the European Union's Horizon 2020 research and innovation program MOPPEX 833460. V. M.R. acknowledges support from the Comunidad de Madrid through the Atracción de Talento Investigador Modalidad 1 (Doctores con experiencia) grant (COOL:Cosmic Origins of Life; 2019-T1/TIC-15379). L.C. has received partial support from the Spanish State Research Agency (AEI; project number PID2019-105552RB-C41). N.H. acknowledges support from JSPS KAKENHI grant No. JP21K03634. P.H. is a member of and received financial support for this research from the International Max Planck Research School (IMPRS) for Astronomy and Astrophysics at the Universities of Bonn and Cologne. K.S. acknowledges the grant MOST 111-2112-M-001-039 from the Ministry of Science and Technology in Taiwan.

This paper makes use of the following ALMA data: ADS/JAO.ALMA#2017.1.00161.L and ADS/JAO.ALMA#2018.1.00162.S. ALMA is a partnership of ESO (representing its member states), NSF (USA) and NINS (Japan), together with NRC (Canada), MOST and ASIAA (Taiwan), and KASI (Republic of Korea), in cooperation with the Republic of Chile. The Joint ALMA Observatory is operated by ESO, AUI/NRAO and NAOJ. The National Radio Astronomy Observatory is a facility of the National Science Foundation operated under cooperative agreement by Associated Universities, Inc.

Facility: ALMA.

Software: CASA (McMullin et al. 2007), `Astropy` (Astropy Collaboration et al. 2013), `MLFriends` (Buchner 2016, 2019), `UltraNest` (Buchner 2021), `SciPy` (Virtanen et al. 2020).

Appendix A
GMC Positions

The GMC positions we have adopted in this analysis (Table A1) are derived from the GMC positions reported by Leroy et al. (2015), which are derived from an analysis of $\sim 1\overset{\prime\prime}{.}5$ imaging of the HCN, HCO^+, and CS 2–1 emission toward the NGC 253 CMZ. The GMC positions listed in Table A1 differ from those listed in Table 3 of Leroy et al. (2015) in two minor ways (A.K. Leroy, private communication):

1. The reference for the offset positions listed in Leroy et al. (2015), Table 3, should be R.A.(J2000) = $00^{h}47^{m}33\overset{s}{.}1442$, Decl. (J2000) = $-25°17'18\overset{\prime\prime}{.}0024$.
2. GMC 5 has been shifted down in decl. by $0.5''$ relative to that reported in Leroy et al. (2015).

The resultant differences between the GMC positions reported by Leroy et al. (2015) and those in Table A1 are less than $1\overset{\prime\prime}{.}5$. The GMC positions listed in Table A1 are also within $0\overset{\prime\prime}{.}5$ of the continuum source positions derived from the 218–365 GHz continuum images presented in Mangum et al. (2019).

Table A1

NGC 253 GMC Positions

GMC	R.A. (ICRS) (00^{h} 47^{m})	Decl. (ICRS) ($-25°$ $17'$)
GMC 1	$32\overset{s}{.}0184$	$28\overset{\prime\prime}{.}248$
GMC 2	$32\overset{s}{.}2776$	$20\overset{\prime\prime}{.}22s$
GMC 3	$32\overset{s}{.}8056$	$21\overset{\prime\prime}{.}552$
GMC 4	$32\overset{s}{.}9736$	$19\overset{\prime\prime}{.}968$
GMC 5	$33\overset{s}{.}2112$	$17\overset{\prime\prime}{.}412$
GMC 6	$33\overset{s}{.}3312$	$15\overset{\prime\prime}{.}756$
GMC 7	$33\overset{s}{.}6432$	$13\overset{\prime\prime}{.}272$
GMC 8	$34\overset{s}{.}0224$	$11\overset{\prime\prime}{.}400$
GMC 9	$34\overset{s}{.}1664$	$12\overset{\prime\prime}{.}264$
GMC 10	$34\overset{s}{.}236$	$07\overset{\prime\prime}{.}836$

Appendix B
GMC 2–5 and 7–10 Model Results

In this appendix, we show modeling results for GMCs 2–5 (Figures B1–B4) and 7–10 (Figures B5–B8) as corner plots. Figure B9 shows observed versus modeled fluxes for the same GMCs.

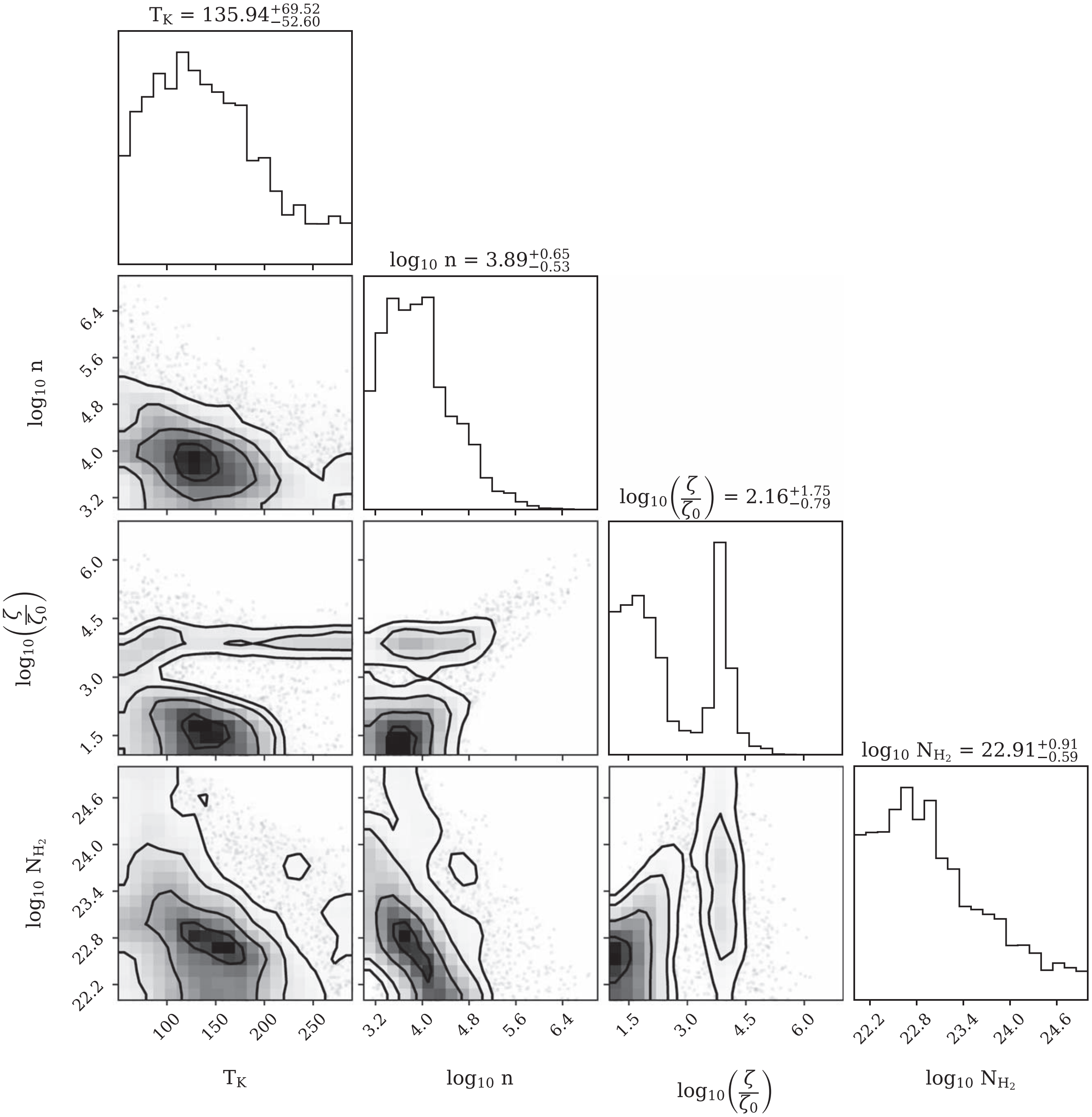

Figure B1. Modeling results for GMC 2.

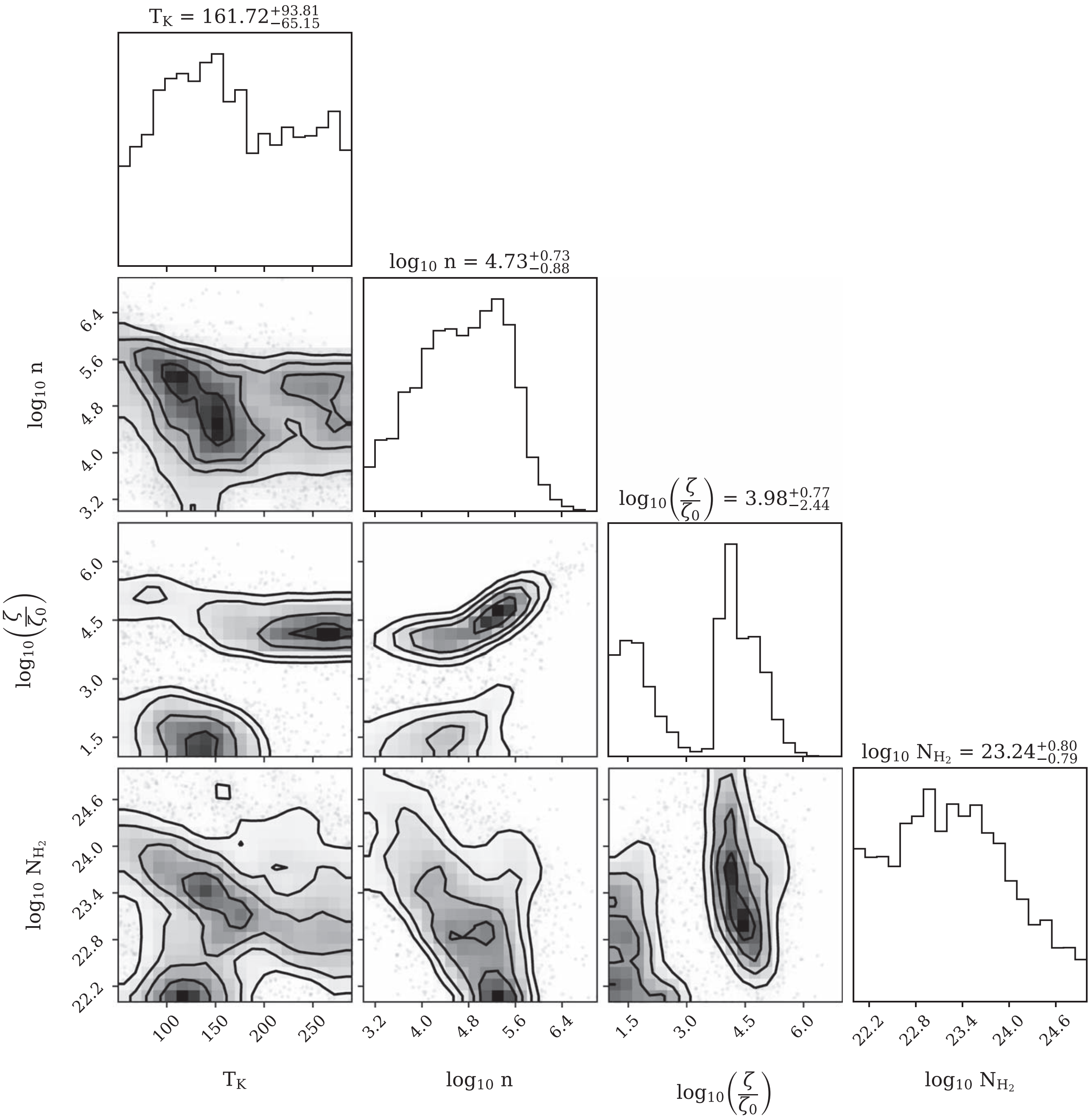

Figure B2. Modeling results for GMC 3.

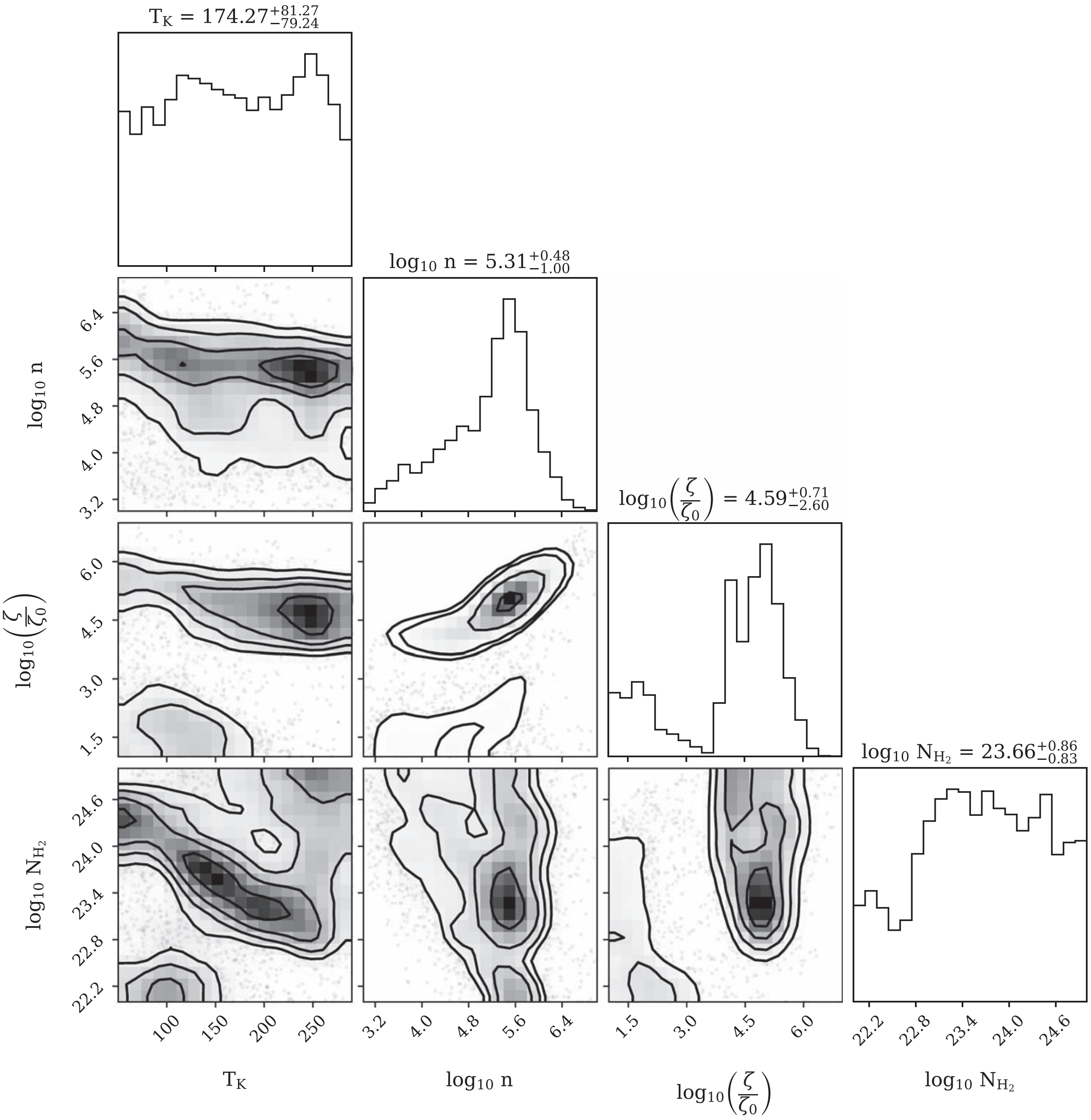

Figure B3. Modeling results for GMC 4.

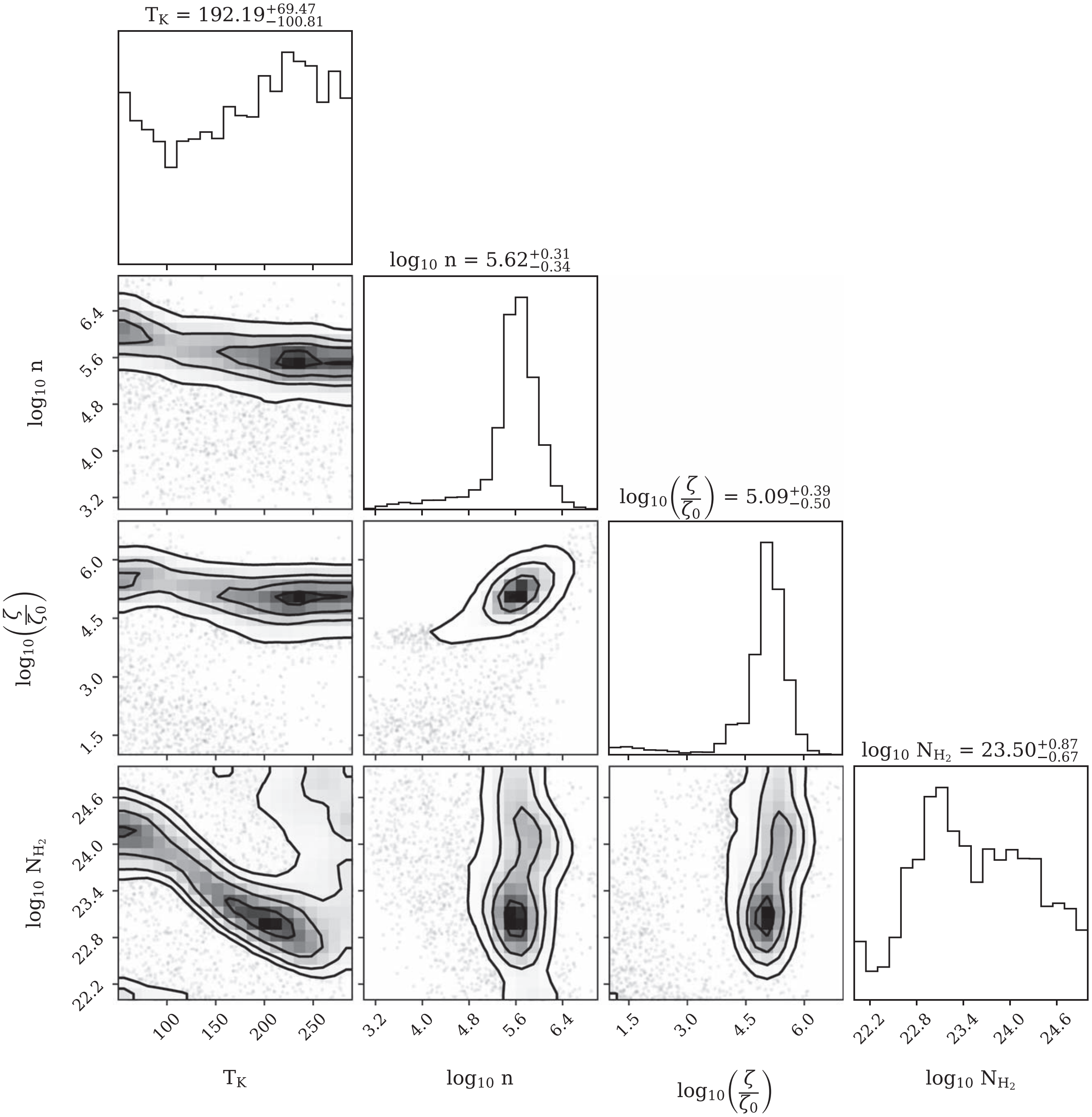

Figure B4. Modeling results for GMC 5.

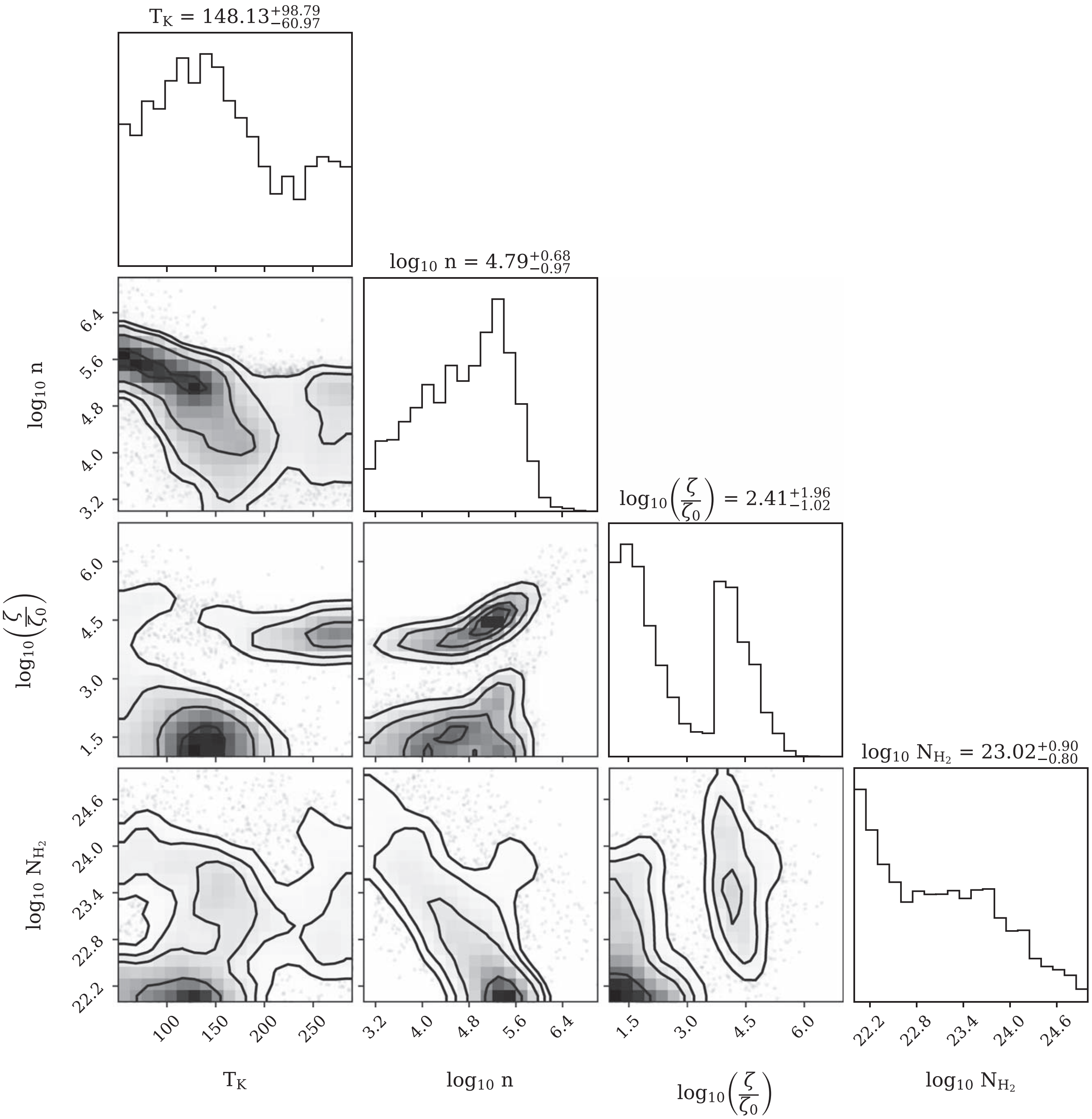

Figure B5. Modeling results for GMC 7.

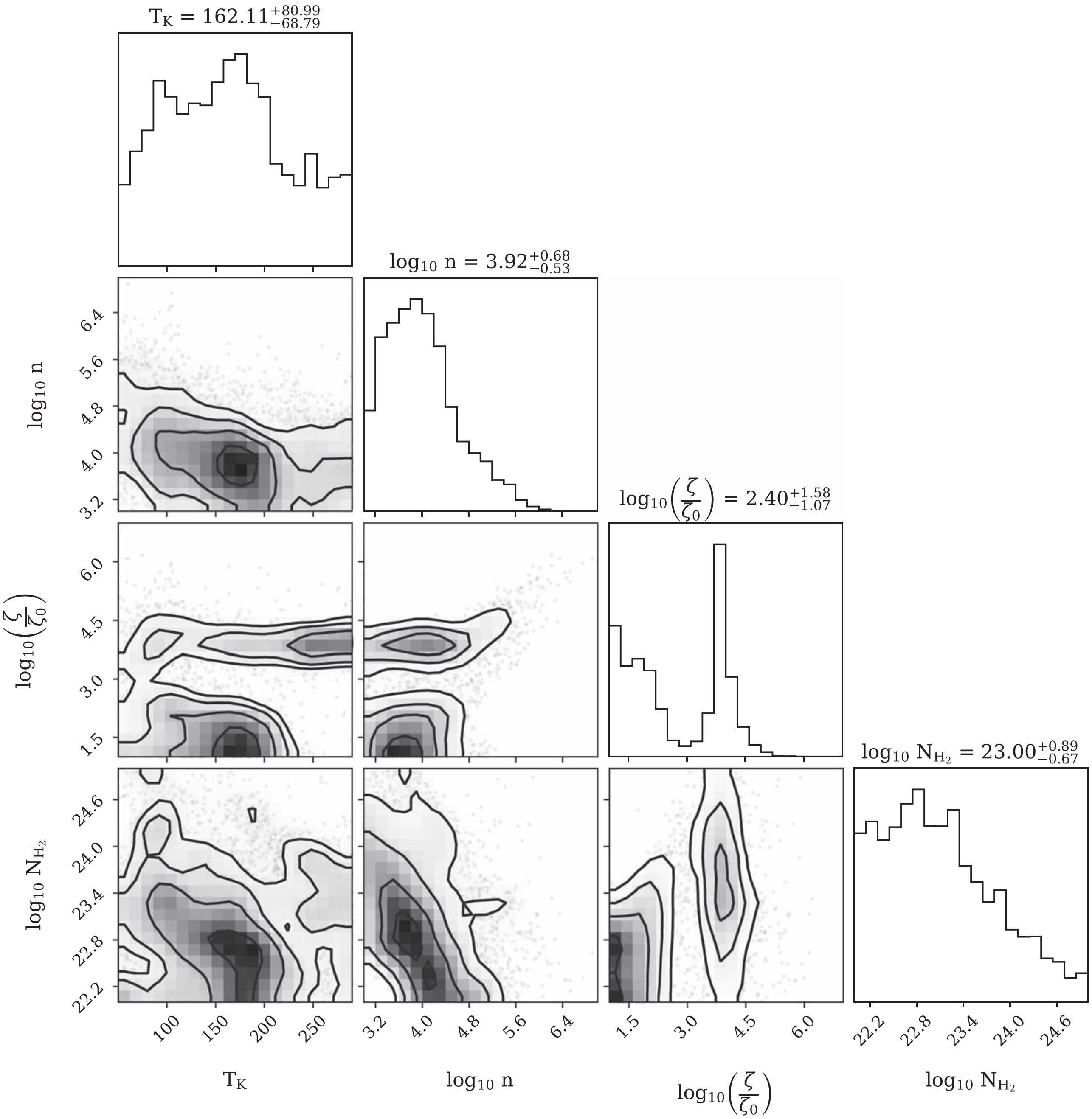

Figure B6. Modeling results for GMC 8.

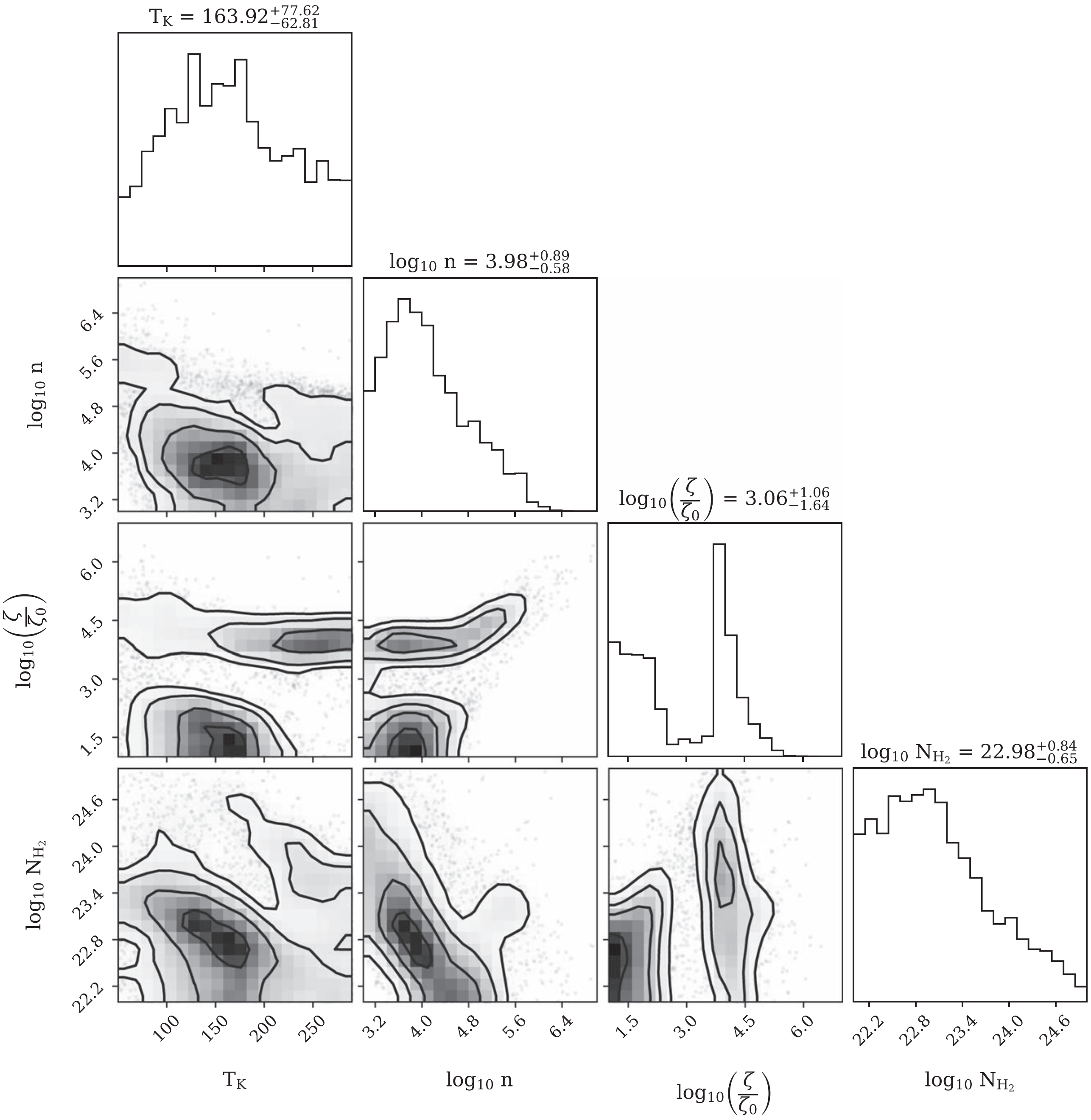

Figure B7. Modeling results for GMC 9.

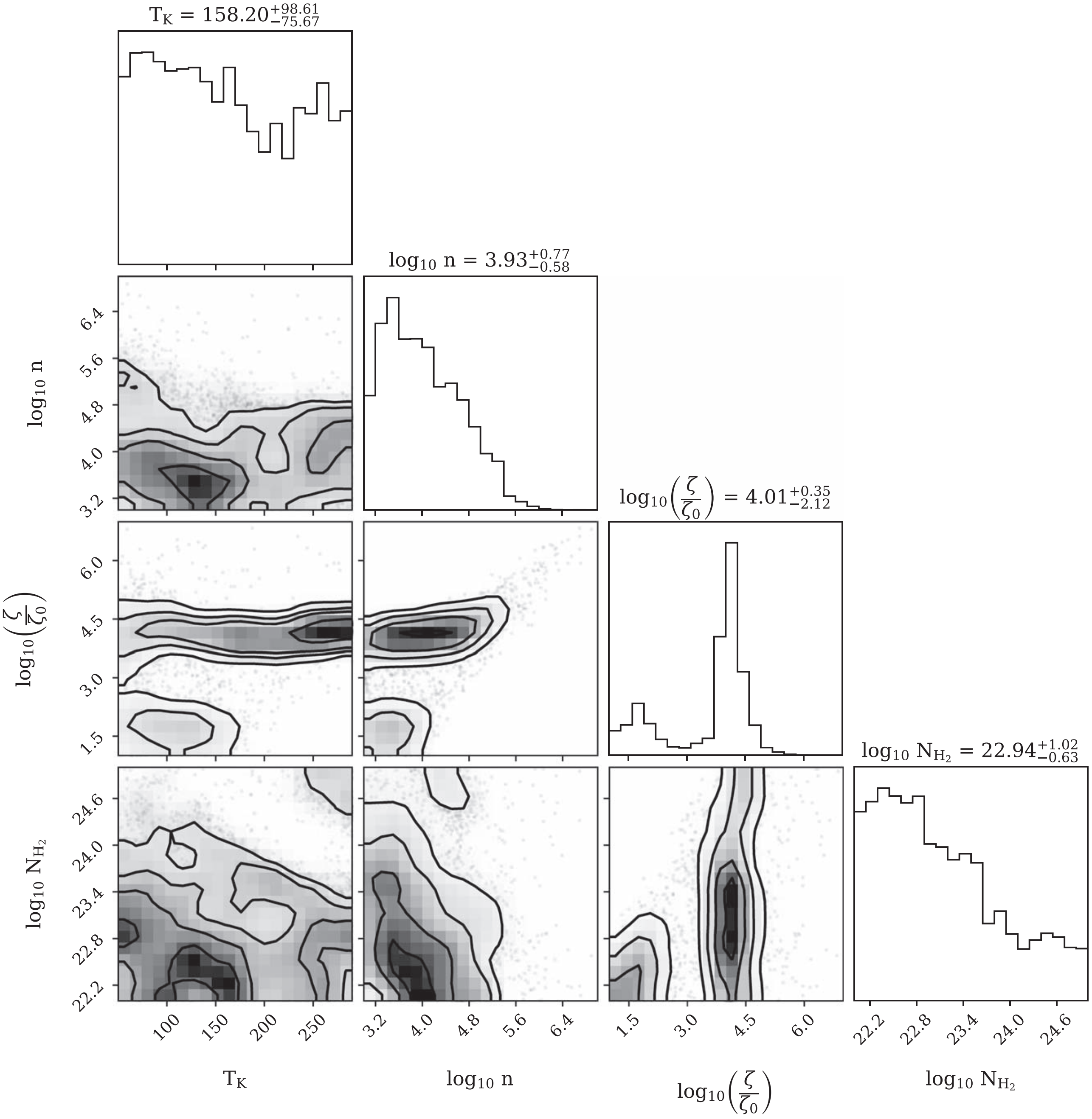

Figure B8. Modeling results for GMC 10.

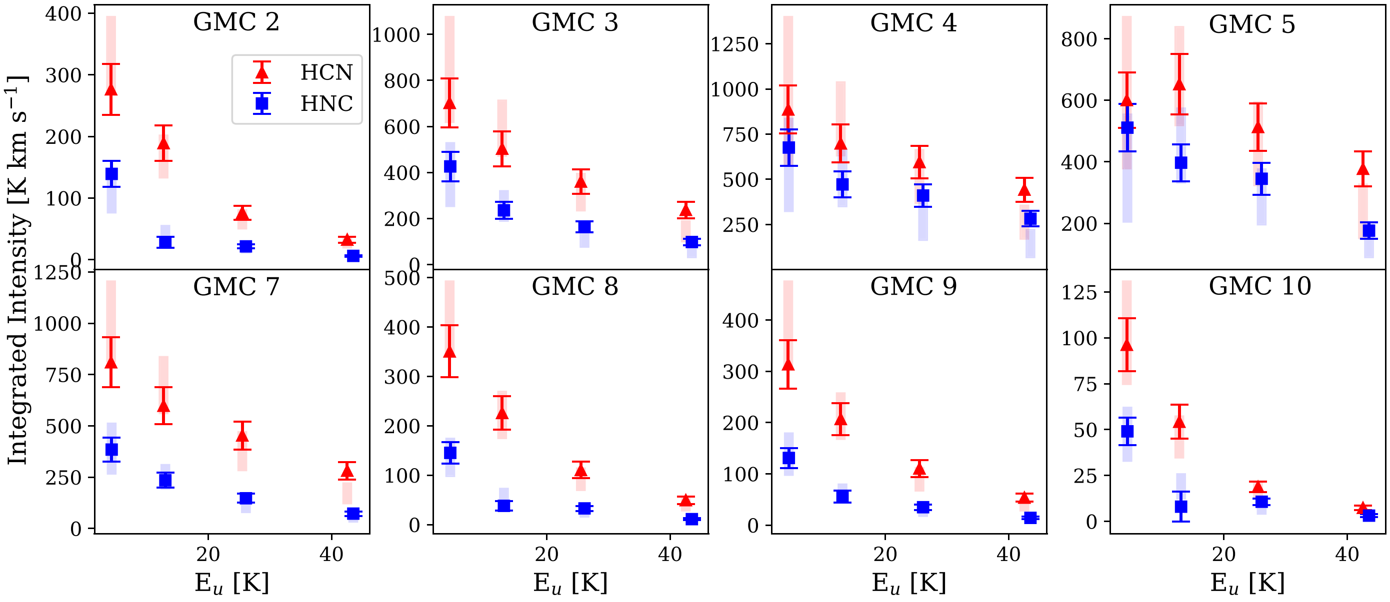

Figure B9. Observed (triangles and squares) vs. modeled (shaded bars) flux for HCN (red) and HNC (blue). Observed error bars indicate the 1σ uncertainty range. Shaded rectangles show the inner 67% (∼16th–84th percentile) of our modeled flux distributions.

ORCID iDs

Erica Behrens https://orcid.org/0000-0002-2333-5474
Jeffrey G. Mangum https://orcid.org/0000-0003-1183-9293
Jonathan Holdship https://orcid.org/0000-0003-4025-1552
Serena Viti https://orcid.org/0000-0001-8504-8844
Nanase Harada https://orcid.org/0000-0002-6824-6627
Sergio Martín https://orcid.org/0000-0001-9281-2919
Kazushi Sakamoto https://orcid.org/0000-0001-5187-2288
Sebastien Muller https://orcid.org/0000-0002-9931-1313
Kunihiko Tanaka https://orcid.org/0000-0001-8153-1986
Kouichiro Nakanishi https://orcid.org/0000-0002-6939-0372
Rubén Herrero-Illana https://orcid.org/0000-0002-7758-8717
Rebeca Aladro https://orcid.org/0000-0002-1316-1343
Laura Colzi https://orcid.org/0000-0001-8064-6394
Kimberly L. Emig https://orcid.org/0000-0001-6527-6954
Christian Henkel https://orcid.org/0000-0002-7495-4005
Ko-Yun Huang https://orcid.org/0000-0002-1227-8435
P. K. Humire https://orcid.org/0000-0003-3537-4849
David S. Meier https://orcid.org/0000-0001-9436-9471
Víctor M. Rivilla https://orcid.org/0000-0002-2887-5859
Paul P. van der Werf https://orcid.org/0000-0001-5434-5942

References

Aalto, S., Garcia-Burillo, S., Muller, S., et al. 2012, A&A, 537, A44
Aalto, S., Monje, R., & Martín, S. 2007a, A&A, 475, 479
Aalto, S., Spaans, M., Wiedner, M. C., & Hüttemeister, S. 2007b, A&A, 464, 193
Aalto, S., Polatidis, A. G., Hüttemeister, S., & Curran, S. J. 2002, A&A, 381, 783
Aladro, R., Martín, S., Riquelme, D., et al. 2015, A&A, 579, A101
Astropy Collaboration, Robitaille, T. P., Tollerud, E. J., et al. 2013, A&A, 558, A33
Bayet, E., Williams, D. A., Hartquist, T. W., & Viti, S. 2011, MNRAS, 414, 1583
Bublitz, J., Kastner, J. H., Hily-Blant, P., et al. 2022, A&A, 659, A197
Buchner, J. 2016, S&C, 26, 383
Goldsmith, P. F., & Kauffmann, J. 2017, ApJ, 841, 25
Buchner, J. 2019, PASP, 131, 108005
Buchner, J. 2021, JOSS, 6, 3001
Costagliola, F., Aalto, S., Rodriguez, M. I., et al. 2011, A&A, 528, A30
Costagliola, F., Sakamoto, K., Muller, S., et al. 2015, A&A, 582, A91
Dalgarno, A. 2006, PNAS, 103, 12269
Dyson, J. E., & Williams, D. A. 1997, The Physics of the Interstellar Medium (2nd ed.; Bristol: Institute of Physics Publishing), doi:10.1201/9780585368115
Ginsburg, A., Henkel, C., Ao, Y., et al. 2016, A&A, 586, A50
Goldsmith, P. F. 2001, ApJ, 557, 736
Goldsmith, P. F., Irvine, W. M., Hjalmarson, A., & Ellder, J. 1986, ApJ, 310, 383
Graninger, D. M., Herbst, E., Öberg, K. I., & Vasyunin, A. I. 2014, ApJ, 787, 74
Green, C. E., Cunningham, M. R., Green, J. A., et al. 2016, MNRAS, 457, 2470
Greve, T. R., Papadopoulos, P. P., Gao, Y., & Radford, S. J. E. 2009, ApJ, 692, 1432
Haasler, D., Rivilla, V. M., Martín, S., et al. 2022, A&A, 659, A158
Hacar, A., Bosman, A. D., & van Dishoeck, E. F. 2020, A&A, 635, A4
Harada, N., Martín, S., Mangum, J. G., et al. 2021, ApJ, 923, 24
Herbst, E., Terzieva, R., & Talbi, D. 2000, MNRAS, 311, 869
Hirota, T., Yamamoto, S., Mikami, H., & Ohishi, M. 1998, ApJ, 503, 717
Holdship, J., Mangum, J. G., Viti, S., et al. 2022, ApJ, 931, 89
Holdship, J., Viti, S., Jiménez-Serra, I., Makrymallis, A., & Priestley, F. 2017, AJ, 154, 38
Holdship, J., Viti, S., Martín, S., et al. 2021, A&A, 654, A55
Humire, P. K., Henkel, C., Hernández-Gómez, A., et al. 2022, A&A, 663, A33
Imanishi, M., & Nakanishi, K. 2013, AJ, 146, 91
Irvine, W. M., & Schloerb, F. P. 1984, ApJ, 282, 516
Jenkins, E. B. 2009, ApJ, 700, 1299
Kamenetzky, J., Glenn, J., Maloney, P. R., et al. 2011, ApJ, 731, 83
Kazandjian, M. V., Meijerink, R., Pelupessy, I., Israel, F. P., & Spaans, M. 2012, A&A, 542, A65
Kokoska, S., & Zwillinger, D. 1999, CRC Standard Probability and Statistics Tables and Formulae, Student Edition (Boca Raton, FL: CRC Press)
Krieger, N., Bolatto, A. D., Leroy, A. K., et al. 2020, ApJ, 897, 176
Le Petit, F., Ruaud, M., Bron, E., et al. 2016, A&A, 585, A105
Lefloch, B., Busquet, G., Viti, S., et al. 2021, MNRAS, 507, 1034
Lenc, E., & Tingay, S. J. 2006, AJ, 132, 1333
Leroy, A. K., Bolatto, A. D., Ostriker, E. C., et al. 2015, ApJ, 801, 25
Leroy, A. K., Bolatto, A. D., Ostriker, E. C., et al. 2018, ApJ, 869, 126
Li, F., Wang, J., Gao, F., et al. 2021, MNRAS, 503, 4508
Mangum, J. G., Ginsburg, A. G., Henkel, C., et al. 2019, ApJ, 871, 170
Martín, S., Mangum, J. G., Harada, N., et al. 2021, A&A, 656, A46
Martín, S., Muller, S., Henkel, C., et al. 2019, A&A, 624, A125
Mauersberger, R., Henkel, C., Weiß, A., Peck, A. B., & Hagiwara, Y. 2003, A&A, 403, 561
McCormick, A., Veilleux, S., & Rupke, D. S. N. 2013, ApJ, 774, 126
McElroy, D., Walsh, C., Markwick, A. J., et al. 2013, A&A, 550, A36
McMullin, J. P., Waters, B., Schiebel, D., Young, W., & Golap, K. 2007, in ASP Conf. Ser. 376, Astronomical Data Analysis Software and Systems XVI, ed. R. A. Shaw, F. Hill, & D. J. Bell (San Francisco, CA: ASP), 127
Meijerink, R., Spaans, M., Loenen, A. F., & van der Werf, P. P. 2011, A&A, 525, A119

Müller-Sánchez, F., González-Martín, O., Fernández-Ontiveros, J. A., Acosta-Pulido, J. A., & Prieto, M. A. 2010, ApJ, 716, 1166
Papadopoulos, P. P. 2010, ApJ, 720, 226
Pérez-Beaupuits, J. P., Aalto, S., & Gerebro, H. 2007, A&A, 476, 177
Rekola, R., Richer, M. G., McCall, M. L., et al. 2005, MNRAS, 361, 330
Rico-Villas, F., Martín-Pintado, J., González-Alfonso, E., Martín, S., & Rivilla, V. M. 2020, MNRAS, 491, 4573
Schilke, P., Walmsley, C. M., Pineau Des Forets, G., et al. 1992, A&A, 256, 595
Spilker, J. S., Marrone, D. P., Aguirre, J. E., et al. 2014, ApJ, 785, 149
Spitzer, L. J., & Tomasko, M. G. 1968, ApJ, 152, 971
Turner, J. L., & Ho, P. T. P. 1985, ApJL, 299, L77
Ulvestad, J. S., & Antonucci, R. R. J. 1997, ApJ, 488, 621
van der Tak, F. F. S., Black, J. H., Schöier, F. L., Jansen, D. J., & van Dishoeck, E. F. 2007, A&A, 468, 627
Virtanen, P., Gommers, R., Oliphant, T. E., et al. 2020, NatMe, 17, 261
Viti, S. 2017, A&A, 607, A118
Webber, W. R. 1998, ApJ, 506, 329